POLITECNICO DI TORINO

Master's Degree in Biomedical Engineering

Master's Degree Thesis

Integration of IMU-based Motion Tracking Algorithms into Wearable Devices for Human Joint Angle Estimation

Supervisors

Prof. Danilo DEMARCHI

Ph.D. Fabio ROSSI

M.Sc. Andrea MONGARDI

Candidate

Silvia TRAVERSO

Torino 21 luglio 2023

Abstract

Motion capture technologies generate real-time data that dynamically represents the position and orientation of a human body in three-dimensional (3D) space. In the clinical medicine and rehabilitation fields, the electromyography (EMG) is commonly used for interpreting patients' muscle conditions but does not give information about the objective performance of movement execution. For this reason, this technique can be combined with motion capture technologies to track patient improvement and guide a therapy. Since the 1980s, many technologies have been tested to track human motion. Visual marker-based tracking systems are considered the gold standard in this field. However, they are expensive and restrict the analysis to a laboratory setting. Inertial measurement units (IMU) are now at the center of the research to overcome these problems. They are light, affordable, and wearable devices that combine accelerometers and gyroscopes. In order to estimate the orientation of an IMU, inertial data can be merged through sensor fusion algorithms. These algorithms integrate gyroscope data and correct the value obtained by observing accelerometer data. The resulting IMU orientation can be expressed as quaternions or Euler's angles. This thesis project aims to integrate an IMU-based motion tracking system into the embedded device designed by Rossi et al. for EMG acquisition. Beyond this analog front-end for bio-signal acquisition, this board contains an IMU module (LSM6DSO32) and a microcontroller (AmbiqMicro Apollo3 Blue). Firstly, the Serial Peripheral Interface (SPI) protocol has been implemented to enable communication between the IMU and the microcontroller, while the Universal Asynchronous Receiver-Transmitter (UART) communication protocol has been used to exchange data and commands between the user interface and the microcontroller. Then, an algorithm to calibrate the IMU has been implemented in the firmware to improve the accuracy of the sensors. A Graphical User Interface (GUI) has been implemented in MATLAB programming language to allow the user to control the system and visualize output data. A validation protocol has been performed by comparing the angles obtained from the relative position of two IMUs with those measured by a modular absolute encoder. Three different Sensor fusion algorithms have been tested and compared in terms of execution time, hardware memory usage, and errors in angle estimation. The comparison of angles obtained from each algorithm has been performed for seven subjects at three different movement velocities and two different starting positions. Under best conditions, we obtained errors of: $9.11° \pm 3.78°$ for the Madgwick algorithm, $8.77° \pm 3.81°$ for the complementary filter, and $16.00° \pm 2.78°$ for the Extended Kalman filter, results that are in agreement with what is reported in literature.

Acknowledgements

ACKNOWLEDGMENTS

"A tutti quelli che mi hanno in qualche modo accompagnato",
Grazie

Table of Contents

List of Figures

Chapter 1

Introduction

In clinical medicine and rehabilitation, accurate assessment and monitoring of patients' muscle conditions and movement execution play a crucial role in guiding therapy and tracking patient improvement. While electromyography (EMG) has traditionally been used to interpret muscle conditions, it does not provide comprehensive information about the objective performance of movement execution. Motion capture technologies have been explored to address this limitation to track and analyze human motion in three-dimensional (3D) space.

Since the 1980s, various technologies have been developed and tested for tracking human motion. Visual marker-based tracking systems have emerged as the gold standard due to their high precision and accuracy. However, these systems are often expensive and confine the analysis to controlled laboratory settings, limiting their accessibility and practicality for clinical applications.

Inertial measurement units (IMUs) have recently gained significant attention in motion tracking research, aiming to overcome the limitations of visual marker-based systems. IMUs are lightweight, affordable, and wearable devices that combine accelerometers and gyroscopes to capture the position and orientation of a human body in real time. Integrating IMUs into rehabilitation therapy monitoring makes it possible to track and analyze the quality and efficacy of patients' movement execution, providing valuable insights for personalized therapy and objective progress evaluation.

To estimate the orientation of an IMU, sensor fusion algorithms are employed to merge the data from gyroscopes and accelerometers. The accelerometer data is combined with gyroscopes' angular velocity measurements to rectify errors or drift in the gyroscopic measures. The resulting IMU orientation can be expressed as quaternions or Euler's angles, providing valuable information about the body's pose and movement.

This thesis project aims to develop a motion tracking system based on IMU technology, which can be seamlessly incorporated into a specialized embedded device

designed specifically for EMG acquisition. The embedded device, developed by Rossi et al., includes an analog front-end for bio-signal acquisition, an IMU module (LSM6DSO32), and a microcontroller (AmbiqMicro Apollo3 Blue). Combining the EMG acquisition capabilities with IMU-based motion tracking, the system aims to provide a comprehensive and holistic approach to monitoring and assessing patients' muscle conditions and movement execution during rehabilitation therapy.

The primary objectives of this thesis are as follows:

Implement the Serial Peripheral Interface (SPI) protocol to establish communication between the IMU module and the microcontroller. Implement the Universal Asynchronous Receiver-Transmitter (UART) communication protocol to enable data and command exchange between the user interface and the microcontroller. Develop an algorithm to calibrate the IMU sensors, improving their accuracy and reliability. Design and implement a Graphical User Interface (GUI) using MATLAB programming language to enable system user control and visualize the output data. Perform a validation protocol by comparing the angles obtained from the relative positions of two IMUs with those measured by a modular absolute encoder, assessing the accuracy of the IMU-based system. Test and compare three different sensor fusion algorithms in terms of execution time, hardware memory usage, and errors in angle estimation, aiming to identify the most suitable algorithm for the given application.

This work is structured into the following chapters:

Chapter 1 provides a comprehensive overview of the concepts necessary to understand the work. It includes discussions on the orientation representation, global coordinate system, Inertial Measurement Unit (IMU), and sensor fusion. These concepts lay the foundation for the subsequent chapters.

Chapter 2 focuses on the various methods commonly used to analyze motion. It explores motion capture technologies and angle measurement technology. This chapter delves into the principles and techniques employed in motion analysis to extract meaningful information from captured motion data.

Chapter 3 provides an in-depth examination of the current state of the art in motion tracking and analysis. It includes a detailed discussion of the devices used for motion capture technologies, angle measurement technology, IMU devices, and the integration of IMU and EMG devices. This chapter explores the advancements and innovations in the field, providing a comprehensive understanding of the current technology landscape.

Chapter 4 presents a thorough description of the system developed for this work.

It provides detailed information about the developed system's design, components, and functionalities. This chapter serves as a guide for understanding the proposed solution's technical aspects and implementation details.

Chapter 5 focuses on discussing, analyzing, and interpreting the results obtained from the experiments and data collection. This chapter presents a comprehensive examination of the findings and their implications.

Chapter 6 represents the conclusion of the work and provides a comprehensive summary of the research study. It reflects upon the achievements, challenges, and limitations encountered throughout the development of the system. The strengths and weaknesses of the developed system are critically evaluated, shedding light on its overall effectiveness and applicability. This chapter also identifies areas for potential improvement and suggests possible solutions or strategies to address them.

1.1 Global Coordinate Systems (GCS)

The coordinate system is a fundamental concept. It provides a standardized reference frame that allows for consistent measurement and interpretation of the position and orientation of objects or bodies. Five different frames are used to characterize and analyze human motions [1]. These frames are illustrated in Figure 1.1 and are described as follows:

1. The inertial frame (I): This frame is centered on the Earth and remains fixed with respect to space. It does not rotate with the Earth's rotation. One of its axes is directed towards the Earth's north pole, while the other two axes lie in the equatorial plane.

2. The Earth's frame (E): This frame is also centered on the Earth but rotates along with its rotation. Its first axis is directed towards the Earth's north pole, while the other two axes align with the east and down directions (NED), respectively.

3. The local coordinate system (L): This frame originates at the center of gravity of the studied mass. It provides a reference system specific to the object or subject under consideration.

4. The body frame (B): This frame is associated with the orientation of the object or subject, represented by a right-handed orthonormal basis (as shown in Figure 1.1). The object's orientation is typically described using Euler angles with respect to the local frame (L).

5. The IMU frame (W): This frame is fixed relative to the body frame (B), although there can be misalignment between them. The Inertial Measurement Unit (IMU) is typically mounted on the object or subject and measures various motion-related parameters.

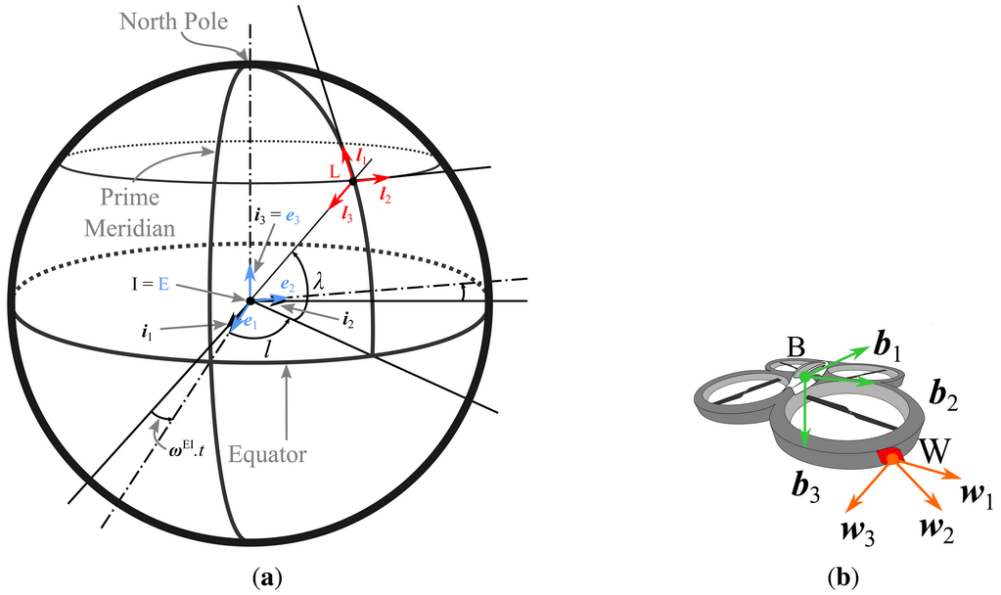

Figure 1.1: Frames illustration: Earth frame (E), inertial frame (I), body frame (B), local frame (L), and work frame (W) [1].

This framework of different frames allows for a comprehensive understanding of human motion by providing reference systems that capture global and local perspectives. Each frame serves a specific purpose in analyzing and interpreting the kinematics and dynamics of human movements.

1.2 Orientation representation

Orientation refers to the spatial position and alignment of an object or coordinates system with respect to a reference frame. It describes the rotational configuration of an object or the relative positions of its axes or components. One common mathematical representation of orientation is rotation matrices, quaternion notation, or Euler angle.

1.2.1 Rotation matrices

Rotation matrices are mathematical representations used to describe the orientation or rotation of an object in three-dimensional space. They are square matrices with dimensions of 3x3, and they contain elements that represent the rotational transformation around each axis (X, Y, and Z) of a coordinate system. A general rotation matrix can be denoted as R and defined as:

$$\begin{bmatrix} r11 & r12 & r13 \\ r21 & r22 & r23 \\ r31 & r32 & r33 \end{bmatrix} \tag{1.1}$$

In this matrix, $r11, r12, r13, r21, r22, r23, r31, r32$, and $r33$ are the elements of the matrix. Each element represents the cosine of the angle of rotation about a specific axis [2].

- $r11$, $r12$, and $r13$: Represent the direction cosines of the X-axis of the rotated coordinate system with respect to the original coordinate system.
- $r21$,$r22$, and $r23$: Represent the direction cosines of the Y-axis of the rotated coordinate system with respect to the original coordinate system.
- $r31$, $r32$, and $r33$: Represent the direction cosines of the Z-axis of the rotated coordinate system with respect to the original coordinate system.

To apply a rotation matrix to a vector representing a point or direction, it would multiply the rotation matrix by the vector using matrix multiplication. Rotation matrices allow for the transformation of coordinates or vectors from one coordinate system to another, reflecting the rotation of an object in three-dimensional space.

1.2.2 Euler's angle

Euler's angles, named after the Swiss mathematician Leonhard Euler, are a set of three angles that describe the orientation of a rigid body in three-dimensional space. They provide a convenient representation for characterizing the rotation of an object relative to a reference coordinate system. The three angles in Euler's angles representation are typically denoted as roll (ϕ), pitch (θ), and yaw (ψ). Each angle represents a rotation around a specific axis in a defined sequence. The sequence of rotations is essential, as different sequences can yield different final orientations [3]. Euler's angles can be defined using an intrinsic or extrinsic rotation sequence. In the intrinsic sequence, the rotations occur with respect to the body-fixed coordinate system. In contrast, in the extrinsic sequence, the rotations are applied relative to the external coordinate system [4]. Conventionally, Euler's angles are defined using an intrinsic rotation sequence. The most common sequence is the ZYX convention,

where the rotation occurs first around the z-axis (yaw), followed by a rotation around the y-axis (pitch), and finally around the x-axis (roll).

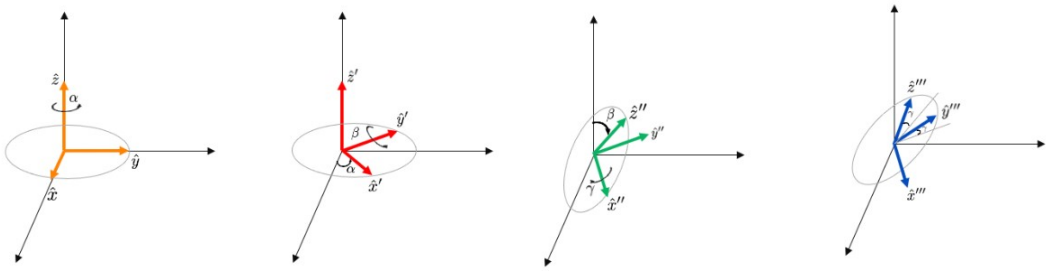

Figure 1.2: ZYX Euler Angle Representation [5]

Mathematically, the rotation matrix R representing the orientation based on Euler's angles can be computed as:

$$R = R_z(\psi)R_y(\theta)R_x(\phi) \tag{1.2}$$

where $R_x(\phi)$, $R_y(\theta)$, and $R_z(\psi)$ are the individual rotation matrices around the x, y, and z axes, respectively

The rotation matrices for each axis can be defined as follows:

$$R_x(\phi) = \begin{bmatrix} 1 & 0 & 0 \\ 0 & cos(\phi) & sin(\phi) \\ 0 & -sin(\phi) & cos(\phi) \end{bmatrix} \tag{1.3}$$

$$R_y(\theta) = \begin{bmatrix} cos(\theta) & 0 & sin(\theta) \\ 0 & 1 & 0 \\ -sin(\theta) & 0 & cos(\theta) \end{bmatrix} \tag{1.4}$$

$$R_z(\psi) = \begin{bmatrix} cos(\psi) & -sin(\psi) & 0 \\ sin(\psi) & cos(\psi) & 0 \\ 0 & 0 & 1 \end{bmatrix} \tag{1.5}$$

Euler's angles have both advantages and limitations. They provide an intuitive representation of orientation and are relatively easy to understand and visualize. However, they suffer from the problem of gimbal lock, which occurs when the pitch angle approaches ±90 degrees. In this condition, two rotational axes align, losing one degree of freedom and ambiguity in the representation. Alternative representations such as quaternions or rotation matrices are often used in applications where gimbal lock and ambiguity are critical concerns to mitigate the limitations of Euler's angles.

1.2.3 Quaternions

In spatial orientation representation, quaternions have emerged as a popular choice for accurately describing the orientation of a sensor. Quaternions being four-dimensional mathematical entities, offer several advantages in terms of stability, efficiency, and computational performance. They allow for seamless interpolation and interpolation between different orientations, making them well-suited for applications involving smooth and continuous motion tracking [6].

A quaternion consists of one real scalar value and three imaginary values.

$$\overline{q} = q_1 + q_2 i + q_3 j + q_4 k \tag{1.6}$$

The letter i,j,k are immaginary number, and follow the rules:

$$ii = jj = kk = -1 \tag{1.7}$$

$$ij = k \tag{1.8}$$

$$ji = -k \tag{1.9}$$

$$jk = i \tag{1.10}$$

$$jk = i \tag{1.11}$$

$$kj = -i \tag{1.12}$$

$$ki = j \tag{1.13}$$

$$ik = -j \tag{1.14}$$

The order of multiplication is significant.

q values are function of the rotaion axis ($\vec{n}$) and the rotaion angle (θ) as shown in the following equations:

$$q_1 = \cos(\frac{\theta}{2}) \tag{1.15}$$

$$\vec{q} = \begin{bmatrix} q_2 \\ q_3 \\ q_4 \end{bmatrix} = \sin(\frac{\theta}{2})\vec{n}, \tag{1.16}$$

$\vec{q}$ is usually reffered to the vector component and q_1 as the scalar component.

Operations:

Quaternion operations involve several mathematical operations such as quaternion multiplication, addition, conjugation, and normalization [6]. These operations allow us to manipulate and combine quaternions to achieve desired results in representing rotations and orientations.

- **Quaternion Addition:**
  Quaternion addition combines two quaternions by adding their corresponding components. The symbol *oplus* denotes it. The addition operation is performed on the real and imaginary parts of the quaternions separately.

  $q \oplus q^{'}$ will result as:

  1. the real component : $q_1 + q_1^{'}$
  2. the imaginary components : $q_2 + q_2^{'}$,$q_3 + q_3^{'}$,$q_4 + q_4^{'}$

- **Quaternion Multiplication:**
  Quaternion multiplication combines two quaternions to produce a new quaternion that represents their composition. The symbol *otimes* denotes it. The multiplication operation follows the Hamilton product rule, defined as:

$$\begin{aligned} q \otimes q^{'} = (q_1 q_1^{'} - q_2 q_2^{'} - q_3 q_3^{'} - q_4 q_4^{'}) + (q_1 q_2^{'} - q_2 q_1^{'} - q_3 q_4^{'} - q_4 q_3^{'})i \\ +(q_1 q_3^{'} - q_2 q_4^{'} - q_3 q_1^{'} - q_4 q_2^{'})j + (q_1 q_4^{'} - q_2 q_3^{'} - q_3 q_2^{'} - q_4 q_1^{'})k \end{aligned} \tag{1.17}$$

- **Quaternion Conjugation:**
  Quaternion conjugation involves negating the imaginary components of a quaternion. It is denoted by the symbol $\overline{q}$. Conjugation is helpful in operations such as inverse quaternion calculation and rotating vectors by quaternions.

$$\overline{q} = q_1 - q_2 i - q_3 j - q_4 k \tag{1.18}$$

- **Quaternion Normalization:**
  Quaternion normalization is the process of scaling a quaternion to have a unit magnitude. The normalization operation ensures that the quaternion remains on the unit hypersphere, and it is essential for maintaining numerical stability in quaternion-based calculations.

$$q_{norm} = \frac{q}{||q||} \tag{1.19}$$

  where q is the quaternion to be normalized and $||q||$ represents the norm or magnitude of the quaternion.

The norm of the quaternion can be calculated using the the Euclidean norm as:

$$||q|| = \sqrt{q_1 + q_2 + q_3 + q_4} \tag{1.20}$$

Once the norm is determined, the normalized quaternion q_{norm} is obtained by dividing each component of q by the norm. This operation ensures that the resulting quaternion has a unit magnitude, making it a valid representation of orientation without scaling effects.

1.3 Inertial Measurement Unit (IMU)

Numerous branches of study frequently focus on the dynamic position of objects (robotics [7], bio-logging [8], UAVs [9], intelligent vehicles [10], medical rehabilitation [11–16], sports learning [17, 18], augmented reality system [19]).
IMU where first used in the 1930s in aircraft navigation [20]. Their usage was restricted to bulk applications due to their limitations, specifically in size, cost, and power consumption.

With the rapid development of Micro Electro-Mechanical Systems (MEMS) technology, low-cost, compact, and low-power sensors became available, providing a more comprehensive range of possibilities in the implementation areas of inertial navigation.

The earlier IMU technology consisted of two types of sensors: accelerometers (used to measure the inertial acceleration) and gyroscopes (used to measure the angular rotation), later this technology progressed with a different sensor type: magnetometer (used to measure the bearing magnetic direction).

1. IMU: This kind of sensor includes an accelerometer and a gyroscope. Typically each sensor has two (if it can measure data along two orthogonal axes) to three (if it measures data along three orthogonal axes: X, Y, and Z) Degrees Of Freedom (DOF). Combining both sensors, the total DOF can range from four to six [21]. The IMU benefits from being immune to interference from external magnetic fields. However, due to sensor noise and the issue with gyroscope drift, relying solely on an accelerometer and gyroscope may not be sufficient to meet measurement accuracy in estimating the object orientation.

2. Magnetic-Inertial Integrated Measurement Unit (MIMU): This kind of sensor includes an accelerometer, a gyroscope, and a magnetometer, commonly all in tri-axial mode to get measurements in a total of nine DOF [21]. This type of sensor is good for dynamic orientation estimation in the short and long run, especially when there are fewer drift errors. However, the accuracy may be

impacted due to the magnetic field disturbance, particularly if the MIMU is used in an environment surrounded by ferromagnetic metal [22].

Several factors must be considered when deciding which type of sensor to use, based on the final usage and tolerance [21]:

1. Package Size: Many products require the sensor to be compact and light to fit the product and have good mobility.
2. Data Accuracy: Some applications only require a limited range of measurements and can tolerate accuracy within a specific range.
3. Response Rate: A suitable sensor should have a fast response rate
4. Degree of Freedom: The DOF determines the number of independent parameters in a system. The number of DOF varies depending on the type of sensors used in the device and the number of axes each sensor will measure. Generally, having more DOF provides additional data and information about the system's motion or configuration. This extra information can lead to a more comprehensive understanding and better estimation of the system's state.

1.3.1 Accelerometer

An accelerometer can be modeled as a second-order spring-mass-damper system (Figure: 1.3).

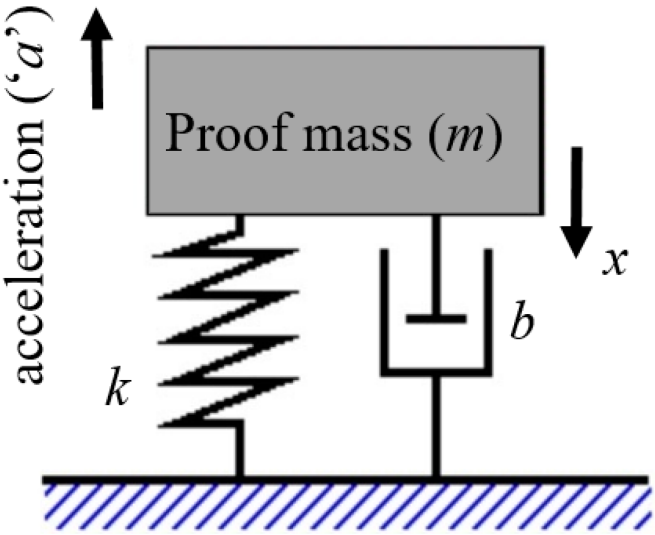

Figure 1.3: Model of accelerometer [23]

with acceleration (a) applied to a mass (m) suspended by a string. The string is characterized by a spring constant (k) and a damping (b). The force applied on the mass is given by:

$$\vec{F}_{applied} = m\vec{a} \tag{1.21}$$

In the system, forces exerted by springs and damping can be defined as:

$$\vec{F}_{spring} = -k\vec{x} \tag{1.22}$$

$$\vec{F}_{damping} = -b\vec{x} \tag{1.23}$$

Using Newton's second law, we get:

$$\vec{F}_{applied} + \vec{F}_{spring} + \vec{F}_{damping} = m\ddot{\vec{x}} \tag{1.24}$$

$$m\ddot{\vec{x}} + b\dot{\vec{x}} + k\vec{x} = \vec{F}_{applied} = m\vec{a}_{applied} \tag{1.25}$$

Equation 1.26 is the transfer function obtained for this system.

$$H(s) = \frac{x(s)}{a(s)} = \frac{1}{s^2 + \frac{b}{m}s + \frac{k}{m}} = \frac{1}{s^2 + \frac{\omega_0}{Q}s + \omega_0^2} \tag{1.26}$$

Where Q is the quality factor, and ω_0 is the resonance frequency.

$$\omega_0 = \sqrt{\frac{k}{m}} \tag{1.27}$$

$$Q = \frac{m\omega_0}{b} \tag{1.28}$$

Given that the accelerometers work in the low frequency domain

$$\frac{x}{a} \sim \frac{m}{k} = \frac{1}{\omega_0^2} \tag{1.29}$$

From this equation, it is clear that there is a tradeoff between bandwidth and sensitivity.

We need a high resonant frequency to have a wide sensing bandwidth, which we can achieve by reducing the proof mass size and increasing the springs' stiffness. However, this reduces the device's sensitivity.

Accelerometers are typically described by their Brownian noise, sensitivity, resolution, frequency response, cross-axis, range, shock resistance, and sensitivity [24].

Brownian Noise

It represents the minimum achievable resolution of an accelerometer. Its equation is given by:

$$B = \sqrt{\frac{a_n^2}{\Delta f}} = \frac{\sqrt{4 \cdot K_b \cdot T_b}}{m} = \sqrt{\frac{4 \cdot K_b \cdot T_w}{m \cdot Q}} \tag{1.30}$$

where Δf is the Bandwidth, K_b is the Boltzmann constant, a_n is the Brownian equivalent acceleration noise and T is the absolute temperature in Kelvin

Sensitivity

An accelerometer's sensitivity is the output voltage value generated per unit input acceleration in g. It is expressed in mV/g. In a triaxial accelerometer, the axial sensitivities are denoted by XS, YS, and ZS and are independent along the X, Y, and Z axes.

$$X_n = \frac{Outpunt\ Voltage\ generated(mV)}{input\ acceleration\ along\ n-axis(g)} \tag{1.31}$$

Cross-Axis Sensitivity

Cross-Axis Sensitivity is usually expressed as a percentage of the sensitivity, and it refers to the output voltage generated by an acceleration orthogonal to a sensitive axis. The Cross-Axis Sensitivity along the n-axis due to the Y-axis is given by:

$$(X_n)_{AY} = \frac{Outpunt\ Voltage\ generated(mV)}{input\ acceleration\ along\ Y-axis(g)} \tag{1.32}$$

Dynamic Range

The accelerometer's dynamic range is the maximum dynamic acceleration value that can be assessed accurately. It is expressed in $'g'$.

Frequency Response and the Bandwidth

This parameter describes how the accelerometer's sensitivity changes as the frequency changes.

Types of Accelerometers

Depending on the transduction mechanism employed to convert the proof-mass shift due to acceleration into a measurable signal, we can have different types of Accelerometers, summarized in Figure 1.4.

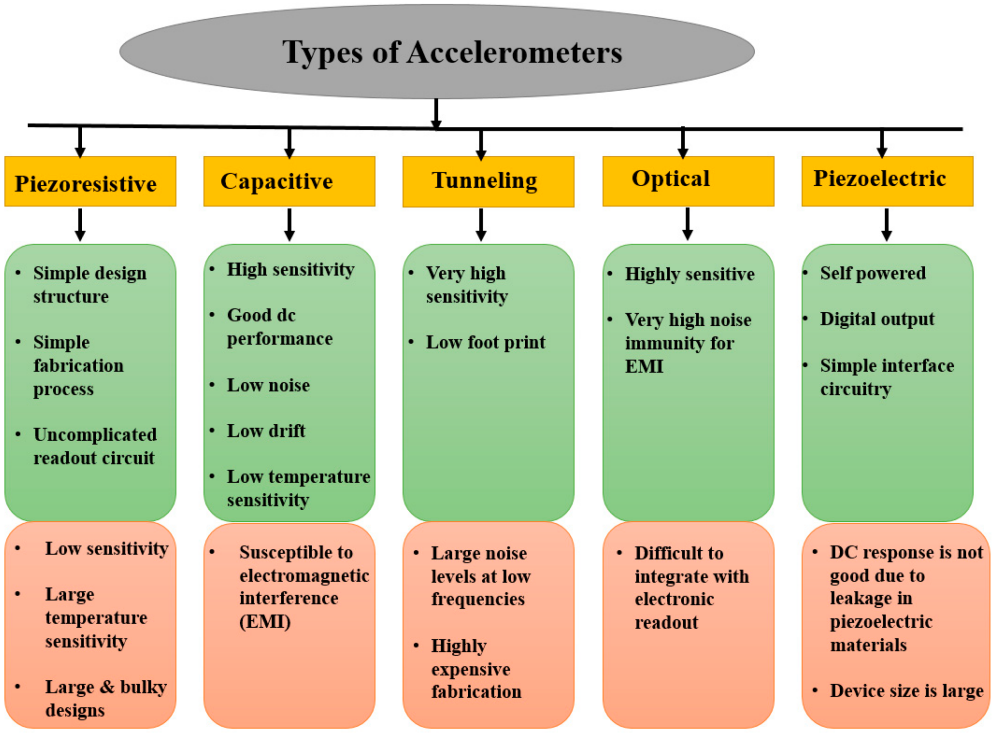

Figure 1.4: Advantages and disadvantages of various types of accelerometers [23]

1.3.2 Gyroscope

A gyroscope is a device used to measure angular velocity. It consists of a spinning rotor that exhibits the property of angular momentum. The gyroscope's principle of operation is based on the conservation of angular momentum.

The rotor is mounted on a set of gimbals that allow it to rotate freely in three axes. When the gyroscope experiences a change in orientation or angular velocity, the resulting gyroscopic effect causes the rotor to resist this change due to its angular momentum. This resistance creates a torque that can be measured and utilized for various engineering applications.

Gyroscopes can be implemented using different technologies, such as mechanical, fiber-optic, or MEMS gyroscopes. Each technology has advantages, limitations, and specific engineering considerations depending on the application requirements.

All MEMS gyroscopes with vibrating elements transfer energy caused by Coriolis acceleration between two vibration modes (Figure 1.5).

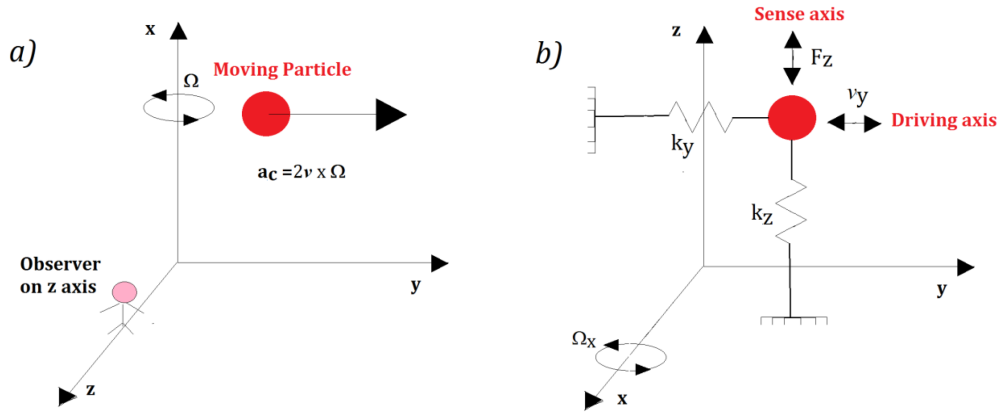

Figure 1.5: particle of mass m moving in space with a velocity v (a) a_c is the Coriolis acceleration acting on a moving particle; (b) mass-spring model of a MEMS gyroscope [24]

Coriolis acceleration refers to an apparent acceleration that occurs due to a reference frame's rotation or relative motion.

Coriolis acceleration arises when an object or a particle moves in a rotating or non-inertial reference frame. As the object moves within this frame, it appears to experience a force perpendicular to its velocity and the rotation axis of the reference frame. This force is known as the Coriolis force. The Coriolis force causes the object to accelerate, and this acceleration is referred to as the Coriolis acceleration [25].

As illustrated in Figure 1.5, the vibrating mass of the MEMS can move through two orthogonal mechanical excitation modes. The master equation results are:

$$m\ddot{\vec{y}} = -k_y\vec{y} - b_y\dot{\vec{y}} + \vec{F}_{Drive} \tag{1.33}$$

Where k_y is the elastic stiffness, b_y is the damping coefficient and F_{Drive} is the applied force.

And

$$m\ddot{\vec{z}} = -k_z\vec{z} - b_z\dot{\vec{z}} + \vec{F}_z \tag{1.34}$$

Where k_z is the elastic stiffness, b_z is the damping coefficient and F_z is the Coriolis force defined as:

$$\vec{F}_z = |2m\vec{\Omega} \times \vec{v}| \tag{1.35}$$

The displacement of mass m along the z direction is governed by the following equation:

$$\Delta z = 2\Omega_x \frac{F_z}{m} \frac{Q_y}{\omega_y} \frac{1}{\sqrt{(\omega_y^2 + \omega_z^2)^2 + (\frac{\omega_y \omega_z}{Q_z})^2}} \tag{1.36}$$

Q_y is the quality factor, and ω_n is the resonance frequency of the driving mode along n.

The sensitivity of a gyroscope refers to its ability to detect and respond to angular velocity or rotational motion. It measures how effectively the gyroscope converts angular velocity into an electrical or mechanical output signal.

As shown in Equation 1.36, the sensitivity of the MEMS gyroscope can be improved by matching the resonant frequencies ω_y and ω_z, and by a decrease of friction (e.g., by creating an under vacuum operating environment).

Gyroscopes are typically characterized by the following issues: Angle Random Walk (ARW), Bias Offset Error, Bias Instability, Temperature Sensitivity, Shock, and Vibration Sensitivity [24].

Angle Random Walk (ARW)

A broadband white noise element, characterized by random fluctuations, is always present in the output of a gyroscope. The ARW parameter describes the magnitude of the noise element's error and can be evaluated using the Allan Variance technique. The Allan Variance is a statistical method used to analyze a gyroscope's stability and noise characteristics. It involves dividing the gyroscope's output data into subsets of varying time intervals and calculating the variance of the differences between successive measurements within each subset. By plotting the Allan Variance against the averaging time, the gyroscope's noise properties, including the ARW, bias instability, and other noise parameters, can be analyzed and characterized. ARW, typically expressed in units of radians per root hour ($rad/\sqrt{hr}$) or degrees per root hour ($^\circ/\sqrt{hr}$), represents the standard deviation of the random noise component per square root of time [26].

Bias Offset Error

The sensor output of a gyroscope can have a non-zero value even when no rotation is applied to the gyroscope. This non-zero output represents the Bias Offset Error, which indicates a systematic error in the gyroscope's measurements. It is commonly expressed in units such as degrees per second ($^\circ/s$) or radians per second (rad/s). The Bias Offset Error is an inherent characteristic of the gyroscope and can be influenced by factors such as manufacturing tolerances, temperature

variations, and aging effects. It is typically specified at a reference temperature, often as $25°C$. Although the Bias Offset Error can introduce inaccuracies in the gyroscope's measurements, it is considered a relatively plain error to compensate for or calibrate. Accurately determining the Bias Offset Error through calibration or estimation techniques can correct this error and enhance the gyroscope's accuracy and reliability in measuring rotational motion.

Bias Instability

Bias Instability is one of the most crucial factors to consider, particularly for long-term acquisition applications. It characterizes the instability of the Bias Offset of a gyroscope under constant temperature and ideal environmental conditions. Bias Instability refers to the gyroscope's tendency to exhibit minor, random variations in its output when subjected to constant input, even without external factors such as rotation. Bias Instability is typically expressed as a root-mean-square (RMS) value in units such as degrees per hour ($°/hr$) or radians per second (rad/s). It represents the magnitude of the fluctuations in the Bias Offset over an extended period. The lower the Bias Instability value, the more stable and reliable the gyroscope's measurements are over time. Various factors, including manufacturing tolerances, temperature variations, aging effects, and other environmental factors, can influence Bias Instability. Minimizing Bias Instability is essential in applications that require precise and accurate long-term measurements, as it ensures the gyroscope maintains a consistent and reliable output under steady-state conditions. Through calibration, compensation techniques, and careful selection of gyroscope components, it is possible to mitigate the effects of Bias Instability and improve the overall performance of the gyroscope, particularly in applications where long-term stability is of utmost importance.

Temperature Sensitivity

Temperature Sensitivity is a measure of the gyroscope's sensitivity to temperature variations. It is typically expressed in units such as degrees per hour per degree Celsius ($°/hr/°C$) or radians per second per degree Celsius ($rad/s/°C$). It represents the rate at which the gyroscope's performance parameters change with temperatures, such as bias offset, scale factor, noise characteristics, and other relevant parameters. Temperature variations can affect the gyroscope's internal components, materials, and electronics, causing changes in its performance. Temperature Sensitivity is a critical factor to consider, particularly in applications where the gyroscope will be exposed to a wide range of temperature conditions. By characterizing and understanding the Temperature Sensitivity of a gyroscope, appropriate compensation techniques or temperature calibration procedures can be implemented to minimize the impact of temperature variations and ensure accurate

and reliable performance across different temperature ranges. This procedure improves measurement accuracy and stability, especially when precise temperature compensation is essential.

Shock and Vibration Sensitivity

Under vibration and shock input, a gyroscope's Bias offset and gyro noise can degrade. Vibration and shock introduce mechanical disturbances that can affect the gyroscope's internal components and sensing elements, leading to changes in its performance. The Bias offset, which represents the systematic error in the gyroscope's output, can be influenced by vibrations and shocks. Similarly, the gyro noise, which represents the random fluctuations in the gyroscope's output, can be exacerbated by vibrations and shocks, leading to increased noise levels and reduced signal-to-noise ratio. Addressing the impact of vibration and shock on the gyroscope is crucial, especially when the gyroscope is exposed to external disturbances or rumors. It may involve implementing mechanical isolation, damping techniques, or protective enclosures to minimize transmitting vibrations and shocks to the gyroscope. This procedure is crucial in applications where precise and consistent motion sensing is required, and external disturbances are prevalent, ensuring that the gyroscope can provide reliable performance even in challenging environmental conditions.

1.4 Sensor fusion algorithms

Sensor fusion is a technique for combining signals from multiple sources better to understand the system in terms of consistency and accuracy.
This approach aims to estimate the IMU's absolute orientation concerning a GCS, typically defined as having a vertical axis aligned with the gravity direction (I). The first step for obtaining a first approximation of the orientation estimate is to integrate the kinematics equation that links the angular rate with the orientation change over time. In the absence of motion, an absolute orientation estimate using only accelerometer measurements can be used to obtain the initial conditions for the integration [2].
The estimated orientation is susceptible to drift due to the integration of the slow-varying bias affecting the gyroscope measurements. The accelerometer measurements can correct this problem, even if they have limitations. Only under static conditions, the accelerometer's estimated inclination is highly reliable.
The vast majority of published Sensor Fusion Algorithms (SFAs) can be divided into two categories: Kalman filters (KF) and complementary filters (CF) [27] [28]. In the last years, numerous formulations of both categories have been proposed, different in the type of orientation representation (quaternions, Euler angles,

rotation matrix, and others) and in the strategy to fuse information (algebraic or optimization) [29–48] Despite numerous research aimed at comparing those algorithms, the literature remains ambiguous about the expected level of accuracy associated with MIMU orientation estimation because contradictory results have been observed ([10, 29, 30, 34, 44, 48–51]). Moreover, the magnitude of errors obtained in comparison studies is typically more significant than that reported in the original algorithm studies. Besides this, errors appear highly variable depending on the experimental setup, algorithm, and commercial device, making it impossible to generalize the results.

1.4.1 Complementary filter

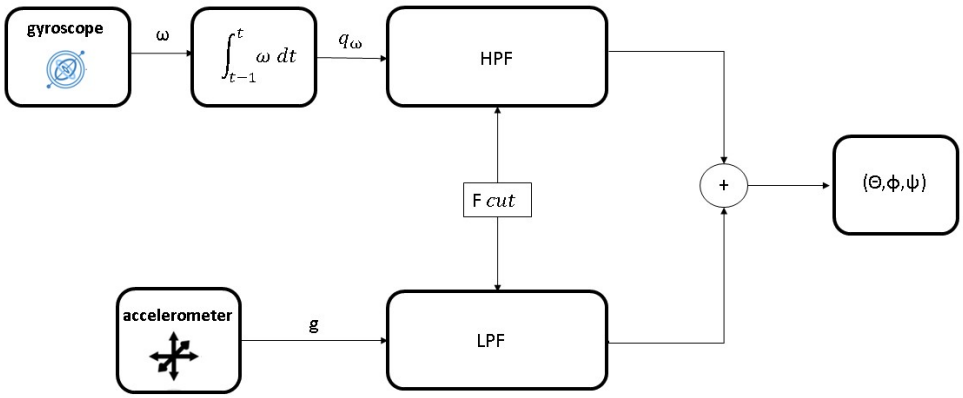

Figure 1.6: Complementay filter block diagram

Complementary filters are considered the simplest solution for combining measurements to estimate orientation accurately (Figure 1.6). They are derived through straightforward frequency analysis and are computationally lightweight and easy to implement [28].

One of the most severe errors affecting its accuracy is bias drift. The bias drift, which has nonlinear characteristics, causes the integration result to drift away from the proper attitude as a function of time, quickly making any calculations useless. This issue is primarily a low-frequency problem.

Conversely, the accelerometer detects centrifugal forces and gravitational force,

resulting in an incorrect attitude determination. Another possible error source is a change in quick-forward acceleration. This type of noise typically has a high frequency. The basic concept of complementary filtering is to combine gyro and accelerometer outputs to estimate the orientation accurately, compensating the drift of the rate gyro with a high pass filter and high dynamics of the accelerometer with a low pass filter. The proper cutoff frequency is used for both sensors. In this way, the final result has the total bandwidth.

The output quaternion, denoted as q, is obtained by combining the gyro and accelerometer outputs according to the equation:

$$q = (1 - \alpha)q_{\omega} + \alpha q_{acc} \tag{1.37}$$

The α parameter is chosen based on which of the two sensors I want to prioritize.

When α is close to 0, the gyro measurements are given more weight, and the orientation estimation relies primarily on the gyro data. This value is beneficial when the gyro is deemed more reliable or when there is a need for a fast response to changes in orientation. However, it can be susceptible to bias drift over time, as gyroscopes are prone to such errors.

When α is close to 1, the accelerometer measurements are assigned more weight, and the orientation estimation depends mainly on the accelerometer data. This parameter is proper when there is a need for a stable and drift-free estimation, as accelerometers are not affected by bias drift. However, accelerometers may be prone to noise and inaccuracies due to external forces or vibrations.

In addition to complementary filters, another popular approach for enhancing orientation estimation is the Madgwick algorithm [52]. Developed by Sebastian Madgwick, this algorithm builds upon the principles of complementary filtering while incorporating sensor fusion techniques to improve accuracy and stability further.

Madgwick filter

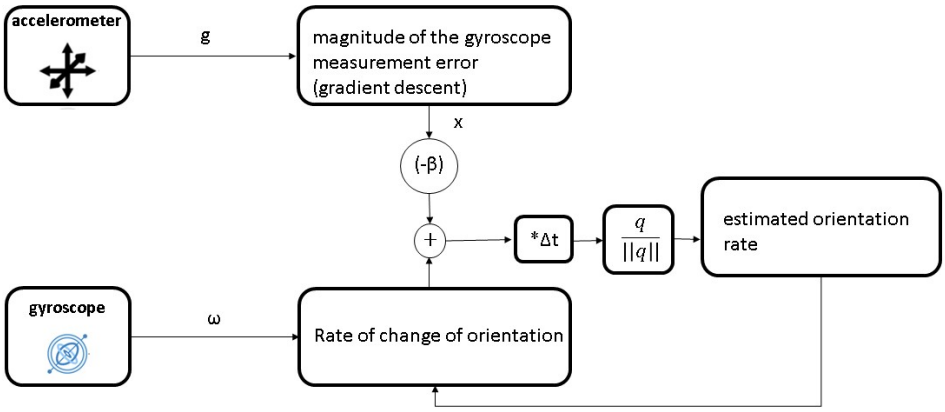

Figure 1.7: Madgwick filter block diagram

Madgwick filter uses accelerometer data in an analytically derived and optimized gradient-descent algorithm to quantify the direction of the gyroscope measurement error [52] .

Essentially, gyroscope estimates of orientation are used as accurate representations in a short time and quicker movements. In contrast, accelerometer data are used as accurate directions to compensate for long-term gyroscope drift through integration.
From the gyroscope, the rate of change of quaternion is obtained with numerical integration [53].
An orientation rate of change is obtained by the accelerometer data using a Gradient Descent algorithm to compute the minimum of the objective function

$$f(q, {}^{E}d, {}^{S}s) = q^{*} \otimes {}^{E}d \otimes q - {}^{S}s \tag{1.38}$$

where

$${}^{E}d = \begin{bmatrix} 0 & d_x & d_y & d_z \end{bmatrix} \tag{1.39}$$

$${}^{S}s = \begin{bmatrix} 0 & s_x & s_y & s_z \end{bmatrix} \tag{1.40}$$

and q is an orientation that aligns any predefined reference in the Earth frame with the sensor frame's. Contributions from the accelerometer and the gyroscope are

then summed

$$q_t = q_{t-1} + (\dot{q}_{gyr} - \beta\dot{q}_{acc}) \cdot \delta t \tag{1.41}$$

Where $\dot{q}_{gyr}$ is obtained from the gyroscope, $\dot{q}_{acc}$ is obtained from the accelerometer, δt is the sampling period, q_{t-1} is the last orientation, and β is an adjustable parameter representing the gyroscope measurement error expressed as the magnitude of a quaternion derivative.

This filter's innovative features are:

1. only one adjustable parameter, its low value gives the gyroscope measurements greater weight.
2. It is based on an optimized and analytically derived gradient descent algorithm, enabling performance even at low sampling rates.

The sources of error include signal aliasing, sensor noise, calibration errors, quantization errors, sensor miss-alignment, and frequency response characteristics [52].

1.4.2 Kalman filter

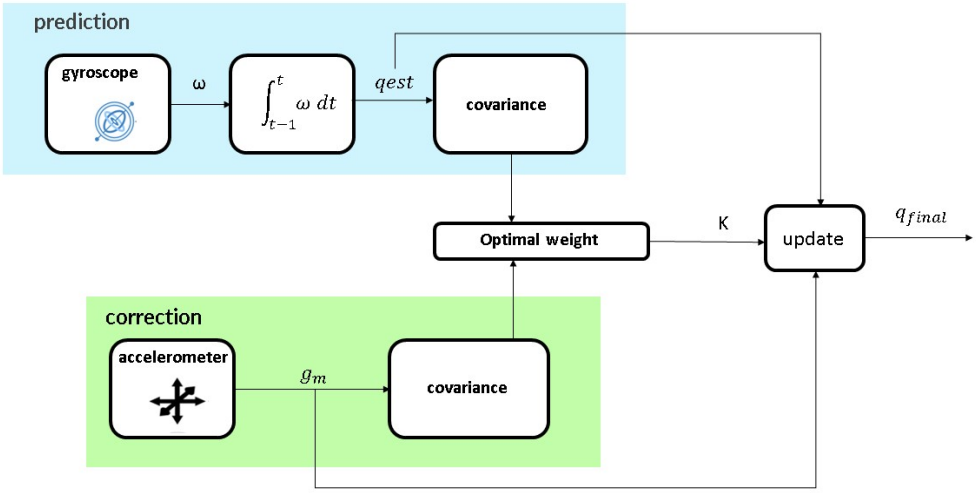

Figure 1.8: Kalman filter block diagram

Kalman filters offer highly accurate orientation estimation and are used in various commercial IMUs [54]. They can accurately estimate orientation in the presence of significant noise sources, such as constant acceleration. On the other hand, Kalman filters are computationally expensive, which might increase hardware costs and latency. They are also challenging to implement. Kalman filter consists of two steps:

1. Prediction step: The system state and the error covariance term is projected forward using the system process model.

2. Correction step: The error covariance calculates a Kalman gain. The predicted state is updated as the difference between the measured state and itself multiplied by the Kalman gain. The Kalman gain is a method of weighing how much the measured values should be trusted compared to the predicted values. If it were a vector of ones, the resulting state would be the same as the purely measured state, and the filter would no longer be recursive. At the same time, if it were a vector of zeros, the resulting state would be identical to the predicted state and completely disregard the measurement. Finally, the error covariance is updated by using Kalman gain information.

This filter is based on two important assumptions:

1. The model is Gaussian
2. All models are linear

If these two hypotheses are correct, Kalman filters provide optimal estimation; if the model is nonlinear, Extended Kalman filters should be used. This filter performs local linearization at each step, using a Taylor approximation of the nonlinear model to convert it into a linear one.

The main idea behind the Taylor approximation is to approximate a function by using its first-order derivative (gradient) and higher-order derivatives (Hessian matrix) evaluated at a specific point.

The linearization process involves selecting a reference point (usually the predicted state) and computing the derivatives of the nonlinear function at that point. These derivatives provide information about the local behavior of the function and are used to construct a linear model that approximates the original nonlinear model.

Chapter 2

Biomechanic application in rehabilitation

Biomechanics plays a crucial role in understanding biological systems by applying mechanical principles. In modern society, the biomechanics of injury, trauma, and rehabilitation has gained significant importance. A key aspect of biomechanics is measuring, evaluating, and assessing human motion. Motion analysis and electromyography (EMG) are fundamental techniques for describing and evaluating human movement.

EMG is a diagnostic tool to assess the electrical activity generated by skeletal muscles. It provides valuable insights into muscle function, activation patterns, and neuromuscular control. EMG is widely employed in clinical and research settings to evaluate muscle performance, diagnose neuromuscular disorders, and guide rehabilitation interventions.

During an EMG assessment, small surface or needle electrodes are placed on the skin above the muscles of interest. These electrodes detect and record muscle fibers' electrical signals during contraction and relaxation. The recorded signals, known as electromyograms, offer valuable information about muscle activation patterns, muscle recruitment, and the timing and intensity of muscle contractions [55].

EMG enables the assessment of various aspects related to muscle function and movement. It aids in identifying muscle weakness, muscle imbalances, abnormal muscle activity, and muscle fatigue. Moreover, EMG signals can be analyzed to determine the timing and coordination of muscle activation, providing insights into motor control and movement patterns.

In rehabilitation, EMG is frequently used to assess muscle function before and after interventions such as exercise programs, physical therapy, or surgical procedures. By monitoring changes in EMG activity, therapists can objectively evaluate the effectiveness of treatments and track patients' progress over time [56].

2.1 Motion catpure technologies

Human motion analysis is the low level-segmentation of the human body into segments connected by joints. In the clinical medicine and rehabilitation fields, motion capture technologies are becoming very popular for measuring the objective performance of the body. Different technologies and techniques have been developed to capture motion Figure 2.1.

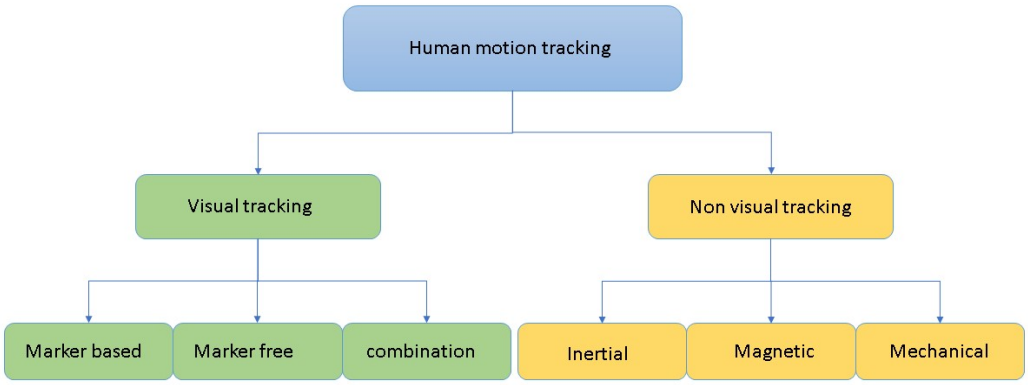

Figure 2.1: Human motion tracking classification based on sensor technologies

2.1.1 Visual tracking systems

Optical sensors (as cameras) are frequently used for motion tracking. Those technologies can be divided into marker-based and marker-less technology, depending on whether they need the application of indicators attached to body parts.

Marker-based visual tracking systems

This technology uses cameras and reflective markers placed on the subject's body to track human movements [57]. The subject is required to wear the marker-based system Figure: 2.2, which can be infrared signal emitters (Active) or just small spheres covered with a reflective material (Passive). Then several synchronized cameras take 2D coordinates (x, y) of each sensor, and by combining those values

for different angles, a 3D (x, y, z) position can be obtained. With all these values, the articular segments of the human body can be rebuilt.
Marker-based technologies are often used as the gold standard for motion tracking because they are very accurate (errors are around 1mm) [58]. Thanks to this high accuracy, this system is widely used in medicine [59] [60]. The use of optical sensors with markers has some significant drawbacks. When the subject is between the camera and the sensor, occlusion issues occur, need a very long and complicated calibration and data elaboration, are very expensive, and can be used only in the laboratory context.

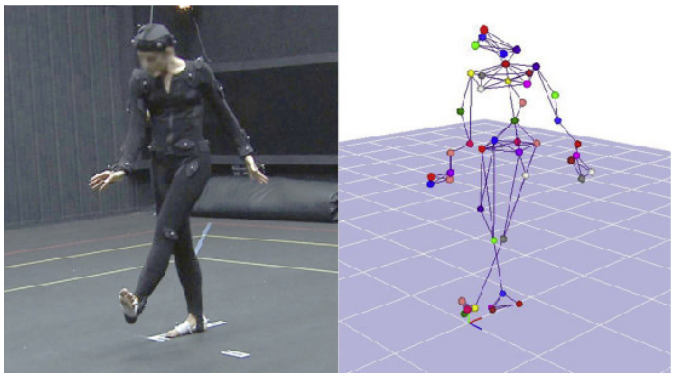

Figure 2.2: Marker-based motion capture technology set-up [61]

Marker free visual tracking systems

In marker-free visual tracking systems, only optical sensors analyze human movement Figure 2.3.
A camera with a million pixels of resolution can accurately detect object movements. Furthermore, cameras can now be obtained cheaply, and the user can configure the camera parameters flexibly. That should make using this technology simple. What is somewhat troubling is that this technique necessitates intensive computation to perform 3-D localization and error reduction, as well as to reduce data latency [62]. Some problems related to marker-free visual tracking systems are the complex environment variability, occlusion, and data volume. Despite much research into marker-free motion capture, only a partial solution has been found to resolve all issues with reasonable computational effort and high accuracy.

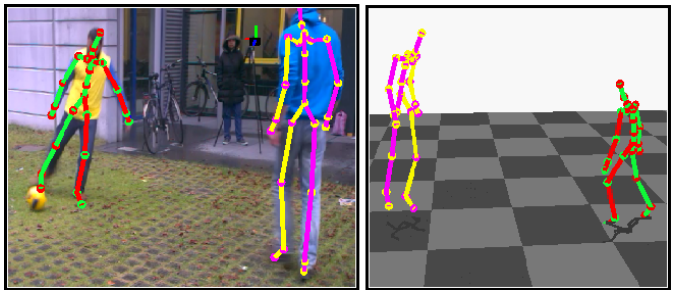

Figure 2.3: Marker free motion capture technology set-up [63]

Combination tracking systems

These systems merge marker-based and marker-free visual tracking systems to reduce errors. The motion templates are constructed using marker-based tracking. These templates are pre-stored in a database and are the source of truth.
The marker-free technique is used to monitor the patient's movements. This strategy necessitates extensive calibration and computing and is still under development [64].

2.1.2 Non visual tracking systems

Non-visual-based tracking devices have been widely deployed because they do not suffer from the "line-of-sight" problem, which cannot be adequately addressed in a residential environment. The "line-of-sight" problem in non-visual tracking systems for motion capture technologies refers to the limitation of these systems in accurately tracking objects or body movements when there is an obstruction or loss of direct visibility between the sensors and the markers on the tracked object.

They employ various technologies, including inertial, magnetic, and mechanical sensing systems.

Magnetic sensors based tracking systems

Magnetic motion capture systems utilize sensors placed on the subject's body to measure the low-frequency magnetic field generated by a transmitter [65]. It reports information about both position and rotation. Three orthonormal coils form the transmitter and generate a magnetic field through a current. The three-orthonormal magnetic-field-strength sensor determines a tracker's absolute position and orientation relative to the source. The distance attenuates the strength of the signal. Pros of this technology are that it is reasonably low cost, has good performance close to the emitter, is small in size, and lacks occlusion. On the

contrary, it has some calibrating problems, operates only on one side of the source, and is affected by ferrous metal and magnetic field [66].

Mechanical sensors based tracking systems

This technology is based on multiple linkage structures and joints. It takes motion information from the mechanical stresses between the linkages. When the patient wears the device, movements cause the mechanical structure to change its angle and strain. The motion is then captured and analyzed based on the angle change measured by the linkage length [67].

Inertial sensors based tracking systems

IMU devices have emerged as a valuable tool in rehabilitation, offering a portable and cost-effective solution for motion capture and analysis [67].

IMU devices provide a range of benefits in rehabilitation settings [68]:

1. Portability: IMU devices are typically compact and lightweight, allowing for easy and convenient use in various rehabilitation settings.

2. Real-time monitoring: IMU devices can provide real-time patient movement feedback, allowing therapists to make immediate adjustments or corrections during rehabilitation sessions.

3. Cost-effective: IMU-based motion capture systems are often more affordable than optical systems, making them more accessible for smaller clinics or rehabilitation centers.

4. Mobility: IMU devices enable motion capture outside a controlled laboratory environment, allowing patients to perform rehabilitation exercises in more natural and functional settings.

However, it is essential to consider some limitations when using IMU devices in rehabilitation:

1. Limited accuracy: IMU devices may have limitations in terms of accuracy compared to optical systems. They can be prone to measurement errors and drift over time, impacting the precision of captured motion data.

2. Sensor placement and attachment: Proper placement and secure attachment of IMU sensors on the body or equipment is crucial to ensure accurate motion capture, which can be challenging, especially for patients with limited mobility or specific conditions.

3. Sensor interference: IMU measurements can be influenced by magnetic fields or electromagnetic interference, potentially affecting the accuracy and reliability of captured motion data.

4. Lack of fine-grained detail: IMU devices may not capture detailed information about joint angles or small movements as effectively as optical systems, limiting the level of analysis and assessment in some cases.

It is important to note that the pros and cons may vary depending on the quality and capabilities of the IMU devices and the specific rehabilitation context in which they are applied. With ongoing advancements in sensor technology and signal processing algorithms, IMU-based motion capture systems are constantly improving, offering valuable insights into patients' movement patterns, progress, and outcomes in rehabilitation.

2.2 Articular angle

In rehabilitation, the assessment and measurement of joint motion play a crucial role in evaluating patients' functional status and progress. One essential parameter used to quantify joint motion is the articular angle. The articular angle is the angular displacement between two body segments at a specific joint. It quantitatively measures the range of motion and the relative orientation of adjacent body segments during movement. The articular angle is typically determined by measuring the angular change between two reference axes or anatomical landmarks associated with the joint of interest [69]. To accurately measure the articular angle, various measurement techniques, and tools can be employed [70]. Traditional methods often involve goniometers, mechanical devices with arms, and a rotating dial that allows therapists to manually align the device with the joint's axes and read the angle directly. However, these manual techniques are prone to human error and may lack precision and reliability. With the advancements in motion capture technology, more sophisticated and precise measurement systems have been developed for assessing articular angles in rehabilitation. Optical motion capture systems that utilize infrared cameras and reflective markers placed on the body segments can provide real-time and three-dimensional measurements of joint angles. These systems offer high accuracy and reliability, allowing therapists to capture and analyze joint motion more precisely. In addition to optical systems, IMUs have also been used to assess articular angles in rehabilitation. The articular angle provides valuable information for clinicians and researchers in the rehabilitation field. It allows for the objective assessment of the joint range of motion, the identification of movement limitations or asymmetries, and the evaluation of treatment outcomes. By monitoring changes in articular angles over time, therapists can track progress, adjust treatment plans, and provide targeted interventions to improve joint function and mobility. It is important to note that interpreting articular angles requires consideration of individual patient characteristics, such as age, gender, joint pathology, and functional goals. Normative data for articular angles can serve as a reference to compare individual measurements and provide insights into the patient's joint motion relative to the general population.

2.2.1 Elbow Angle

Elbow movements are described in the literature in terms of flexion and extension [71].

For everyday activities, elbow angles have been observed from 0 to 150° [72]. Angles from 130° up to 150° are required in tasks related to personal care, for example, hair care and face washing, as well as eating or drinking. Angles from 0° up to 20° are necessary for tasks such as reaching and touching one's toe, which

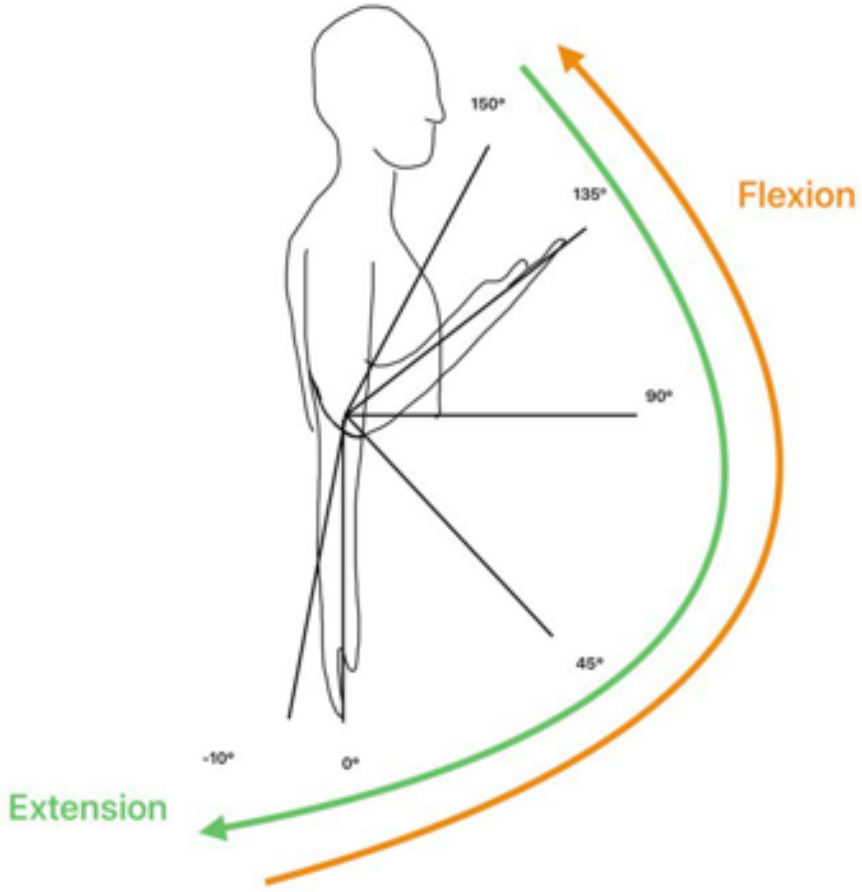

Figure 2.4: Elbow angle flexion end Extention

embodies putting on shoes and socks.

2.3 Angle Measurement Tecnology

In rehabilitation medicine, measuring a joint angle is a standard clinical measurement technique used to track patients' improvement, evaluate the efficacy of care, and guide therapy. The literature for this purpose includes various techniques, including analyzing x-ray images [73], encoders [74], universal goniometers [75], motion capture technologies [76], and inertial sensors [77].

2.3.1 x-ray fluoroscopy images

This technology allows the real-time visualization of bone motion. The generator produces an X-ray beam that irradiates the target joint, while an image intensifier converts the X-ray beam into a light signal (radiograph) [73]. Most x-ray fluoroscopy systems limit the analysis to laboratory settings, and only restricted motions can be analyzed.

2.3.2 Encoders

Encoders are the most frequently used strategy for joint angle estimation. We can distinguish between magnetic rotary encoders [74], and optical rotary encoders [78] based on the technology applied.

Magnetic encoders

Two pieces are often included in magnetic encoders, one on each link on the joint. A multipole magnet and a Hall-effect sensor are the two components that go together, and they need to be tightly connected (within a distance of a few millimeters) [74]. Magnetic encoders typically produce results for angles with modest resolution (8–12 bits); they are inexpensive, all-purpose, contactless, highly dependable, and have long lifetimes. These sensors' drawbacks include the need for direct-current magnetic shielding and particular magnet coupling alignment, which can result in pricey mechanical coupling and packaging design.

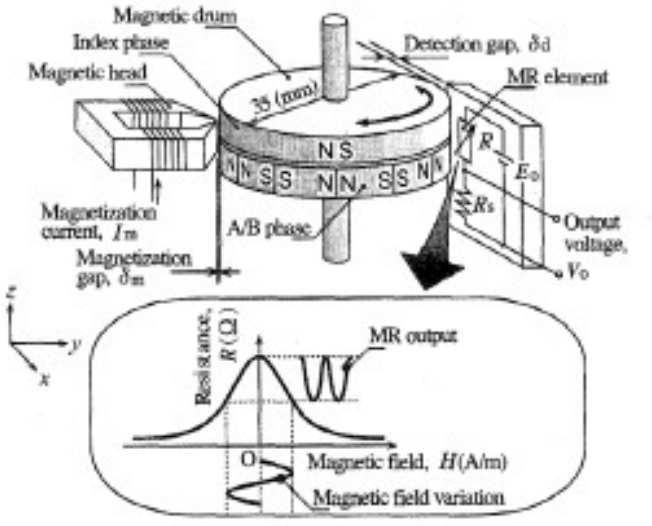

Figure 2.5: Magnetic encoder, structural view

Optical encoders

Optical encoders have two pieces, one mounted on each connection [78]. The disk in one part has a window edge that has been precisely cut, and a photodetector and a light source in the other portion detect the disk's relative angle.
Optical encoders can typically produce angular outputs with a significantly greater resolution (up to 30 bits) than magnetic encoders. Although they can be pretty accurate, they can be very costly and more susceptible to the effects of the environment (vibration, shock, stress).

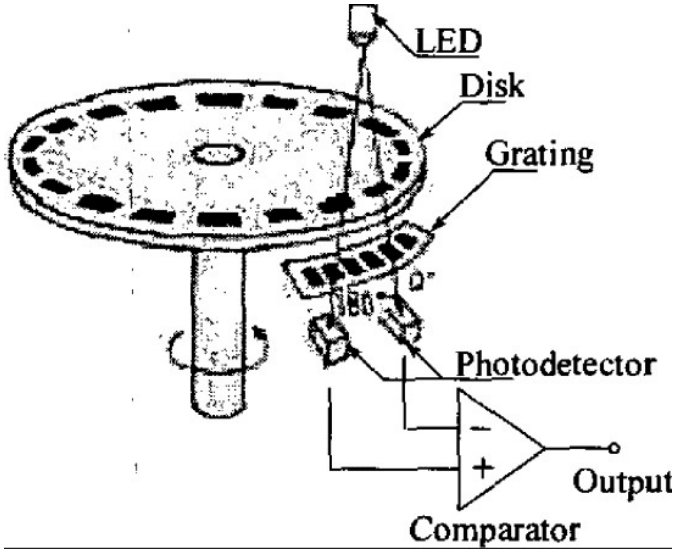

Figure 2.6: Optical encoder

2.3.3 Universal Goniometer

The goniometer is the most straightforward and versatile tool for determining ROM in clinical practice.
It was designed around 60 years ago. Thanks to its adaptability, it quickly became a helpful evaluation tool in physiotherapy and rehabilitation [75]. Nonetheless, several authors doubt the universal goniometer's poor intertester reliability. Furthermore, doctors note difficulties linked to this technology, including the need to hold the goniometer's arms while taking a measurement, their stabilization throughout the readout, and problems locating landmarks on the patient's body. The inclinometer, often known as the digital version of the universal goniometer, is its progression. Kolber et al.[79] studied the validity and reliability of active shoulder elevation employing a digital inclinometer and goniometer. The results support the interchangeable use of goniometry and digital inclinometer for measuring scaption

[80].

2.3.4 Optical motion capture systems

Motion capture systems have effectively characterized joint kinematics by monitoring the relative motion of contiguous body segments [76].

These procedures show problems linked to intrinsic marker movements with the underlying bones. Numerous strategies have been put out to solve this issue. There are two main approaches: joint constraints, which optimize relative segment orientation and position [81], and local or segmental methods, which account for the relative movements of the markers attached to a body segment as a cluster [82]. The use of these systems is constrained by their high cost, need for controlled laboratory environments, occlusion problems, and risk of skin movement artifact [83].

2.3.5 IMU based motion capture systems

MIMU sensors started to become popular to overcome problems associated with the other motion measurement techniques, initially only to detect two degrees of freedom movement in controlled activities. Many solutions have been proposed through the years. At first, it used only accelerometer measurement with the equation

$$\theta = (180/\pi \arcsin(a_z/g)) \tag{2.1}$$

where a_z is the accelerometer measured along the z-axis.

This solution, however, is reliable only if the subject is still. Dejnabadi et al. proposed a new method based on gyroscope integration, but the results were distorted because of the problem of offsets and drift [77].

Another work by Dejnabadi et al. proposed computing the angular displacement using angular velocity and acceleration measures and switching between the two sensors following the wave frequency of the body segment [84]. Unfortunately, obtaining a precise switching frequency resulted to be challenging.

Karol et al. [85] proposed a solution based on three sensors: an accelerometer, a gyroscope, and a magnetometer. However, this first study was only based on static acquisition (there was no linear acceleration or global rotation).

Several sensor fusion algorithms currently combine accelerometer, gyroscope, and magnetometer values to obtain the orientation of the MIMU in space. Joint angles can be estimated by applying two or more MIMUs on the subject and computing the relative position. Since all these approaches have limitations, they are constantly evolving.

Chapter 3

State of Art

3.1 Motion capture technologies

This paragraph presents some of the devices currently used for motion capture on the market.

3.1.1 Marker-based visual tracking systems

Qualisys is a Marker-based visual tracking system based on passive markers, composed of 1 to 16 cameras, each producing an infrared light beam [86].
A similar device called VICON was created especially for immersive and virtual settings [87] [88]. They allow the creation of an optimal system. The user can choose between four cameras and ten different marker types.
CODA is an active marker device. This system can track 360° movements when up to six sensor units are utilized together. Active markers can be detected by their placements during a time-multiplexed sequence. CODA has been frequently used as the gran truth in the medicine field [89]. This device was also used for a dynamic polyelectromyographic assessment of muscle spasticity and overactivity, as well as Motion Analysis for Treatment Planning [90].
Another active marker device is Polaris, produced by Northern Digital Inc. [91]. This device is beneficial when lighting is not steady; indeed, it comprises position sensors, combined with passive or active markers that can be used up to the subject.

3.1.2 Marker free visual tracking systems

Microsoft Kinect is one of the commercial devices used for marker-free motion analysis. It was first designed for gaming but lent itself to different applications. Kinect v1 comprises one IR emitter, one IR camera, and one RGB camera that allows the acquisition of depth and color of the image. Kinect v1 accuracy was

proved to be affected by sunlight.
A second version of the device (Kinect v2) was released with improved RGB and IR cameras. In this version, a time-of-flight (TOF) technology is applied to measure the depth of the schene. This device provides a three-dimensional skeleton of 25 joints. Kinect v2 improved motion capture accuracy compared to the previous version, especially in outdoor measurements.

Another marker-free device for motion analysis is the one developed by The Captury. This technology allows the acquisition of up to 3 people with 6 to 24 cameras controlled by a computer. It can be used indoors and outdoors. The background can be dynamic without specific light conditions.

BioStage's device made up of 8–18 cameras (120 fps in real-time), is only usable in a laboratory setting.

Another device available for markerless motion analysis is Shape 3D. This device is made up of up to 8 high-speed color cameras. It can be used for outdoor measurement, but optimal acquisition requires a stable background with good contrast.

Magnetic sensors based tracking systems

The Ascension Technology Corporation in the United States has produced a magnetic motion capture device called MotionStar 3.2. This system uses dc magnetic tracking technologies, which are less prone to metallic distortion than ac electromagnetic tracking techniques. It shows some excellent performance as translation range: $\pm 3.05m$; angular range: all attitude $\pm 180°$ for Azimuth and Roll, $\pm 90°$ for Elevation; static resolution (position): $0.08cm$ at $1.52m$ range; static resolution (orientation): $0.1RMS$ at $1.52m$ range [92].

Another device on the market is the one from Polhemus: LIBERTY Figure 3.1. LIBERTY is the quickest and most precise electromagnetic tracker currently on the market. It represents a quantum leap in six-degrees-of-freedom tracking technology (computed at 240 updates per second), has virtually no latency, and offers a precision of $0.03RMS$ for X, Y, and Z position and $0.15°RMS$ for orientation, which is remarkably accurate.
A different device was created by Caruso, which implemented a new compass to accurately identify the heading, using solid-state magnetic and a tilt sensor [93].

Figure 3.1: liberty magnetic tracker by Polhemus

Figure 3.2: MotionStar DC magnetic tracker by Ascension Technology Corporation

Mechanical sensors based tracking systems

Gypsy Torso Figure 3.3 by Meta Motion is an example of a motion capture upper body solution that provides real-time performance with minimal latency. It can be connected via serial cable to a PC / laptop. Another Device, also from Meta motion, is Gypsy 7. It is a total body device with 14 joint sensors and an accuracy of 0.125 degrees resolution. USB-powered does not need a battery. It weighs 4 Kg.

In 1998 Andersen designed one of the first gloves (the CyberGlove) based on Mechanical sensor technology [94].

Figure 3.3: Gypsy 7 Torso Motion Capture System

Figure 3.4: CyberGlove

3.2 Angle Measurement Tecnology

A summary of the technology used for Angle measurement will be presented in this paragraph.

3.2.1 x-ray images

Bey et al. validated the accuracy of using x-ray images for determining the in-vivo shoulder's glenohumeral joint translations motion [95] based on their three-dimensional shape and texture. The accuracy of this strategy before was only tested in cadavers by Bey et al. [96]. They acquired X-ray images at $60Hz$ while the subject performed two tasks. After examination, complete bilateral CT images of the scapula and humerus were obtained. Using a model-based tracking technique, the biplane X-ray images of the humerus and scapula were used to identify their 3D position and orientation. This technique allows the detection of a bone's position and orientation based on optimizing the correlation between two digitally reconstructed radiographs and the two biplane X-ray images. The motion of the humerus about the scapula was estimated using all six kinematic parameters (three rotations and three translations) to characterize joint motion. As a result, they obtained an accurate and non-invasive technique for joint angle estimation. While the rotations of the glenohumeral joint observed in this investigation are consistent with earlier studies, these systems are restricted to static or very slow and limited ranges of motion, requiring a dedicated laboratory and skilled personnel to run the equipment.

3.2.2 Encoders

Since encoders are used for many different applications besides medicine, many different devices are available on the market.
For rehabilitation purposes, encoders have been used mainly in two ways: in digital goniometers and Exoskeleton.

Dominguez et al. developed a digital goniometer using encoders to measure the knee-joint angle. They use a contactless magnetic absolute encoder AS5040 (Austria Microsystems ®, USA) [97]. This encoder converts angular position into binary code with a 10-bit resolution. The encoder is mounted in the middle of two aluminum bars, Figure 3.5

Lee et al. developed a Lower-Limb Exoskeleton Robot Figure 3.6 for continuously estimating the knee and ankle angle during walking. Exoskeleton has 1 degree of freedom for the knee and 2 degrees of freedom for the ankle. To measure angles, they use a 12-bit absolute encoder (AMT 203-V CUI Inc., Gyeonggi-do, Korea) to

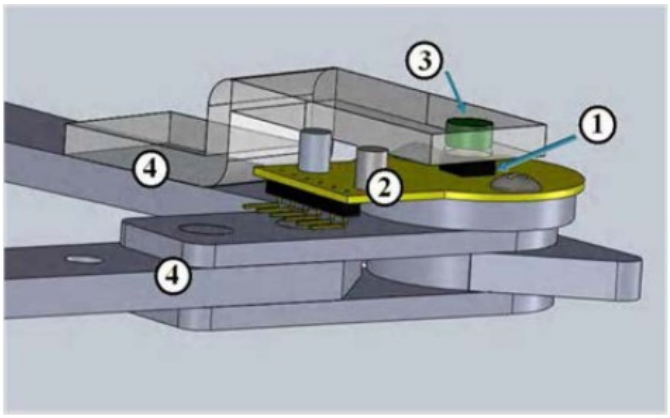

Figure 3.5: Digital goniometer, using encoder

give values from 0 to 360 degrees. In addition, an IMU device (EBIMU-9DOFV5 IMU) was added to collect accelerometer and gyroscope data.

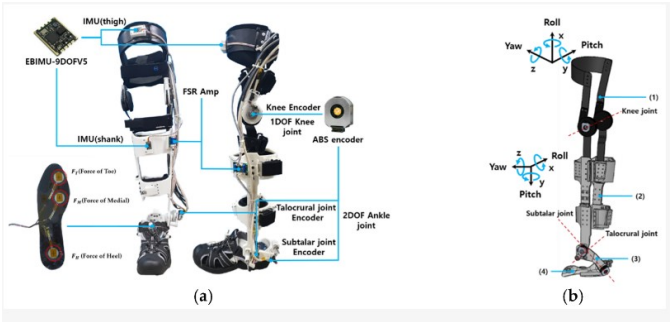

Figure 3.6: Exoscheletum for knee and ankle joint angle acquisition. a) is the final device, b) is the 3D modeled device.

3.2.3 Universal goniometer

Universal goniometers are affordable instruments that can also be purchased not from specific retailers. Figure 3.7 is an example. This device allows the acquisition of values from 0 to 360 degrees whit a precision of 1 degree. It is made of plexiglass and is 3mm thick and 30 cm long.

A different technology is used in Halo device 3.8. This digital goniometer can measure every joint angle while being pocket size. It allows the accuracy of up to 1 degree in 5 seconds. It can be used with only one hand and record previous measurement values.

Figure 3.7: universal goniometer for anthropometric measurements

Figure 3.8: Halo device for anthropometric measurements

3.3 MIMU devices

There are a variety of IMU-based sensors available on the market.

1. MTw Figure 3.9, is a computerized acquisition device that measures the earth's magnetic field, acceleration, and 3-D rate of turn created by Movella [98]. Sensors full scale are $\pm 2000 deg/s$, $\pm 160 m/s2$, $\pm 1.9 Gauss$ This device has the dimension of $47 \times 30 \times 13 mm$ for $16g$ of Weight, allows the connection of up to 34 sensors simultaneously, and synchronization with third-party devices. The MTw system has $0.05^{\cdot}$ root-mean-square (RMS) angular resolution, $1^{\cdot}$ static accuracy, and $1.5^{\cdot}$ RMS dynamic accuracy in a uniform earth-magnetic field.

Figure 3.9: MTw mimu sensors for tracking human motion

2. 3DMGQ7 Figure 3.10 from Parker device is a solution with a centimeter-level position accuracy, with low drift and low noise MEMS inertial sensor [99]. This device has the dimension of $76mm \times 68.6mm \times 13.3mm$ for a $78grams$ weight.

Figure 3.10: 3dmgq7 mimu sensors for tracking human motion

3. APDM-OPAL Figure 3.11 is a device with the dimensions of $43.7 \times 39.7 \times 13.7mm$ for $25grams$ of weight. It comprises two accelerometers, a gyroscope,

and a magnetometer. Sensors have a Range of $\pm 16g$, $\pm 200g$, $\pm 2000deg/s$, $\pm 8Gauss$.

Figure 3.11: APDM-OPAL mimu sensors for tracking human motion

4. Shimmer3 Figure 3.12 is a commercial $51mm \times 34mm \times 14mm$ device, sensors implemented have range of $\pm 16g$, $\pm 2000deg/s$, $\pm 4Gauss$.

Figure 3.12: Shimmer3 mimu sensors for tracking human motion

3.4 IMU and EMG devices

3.4.1 Wearable inertial data and muscle activity monitoring

As described in the sections above, measuring joint angle and EMG is of great clinical interest. It has also been proved that monitoring participants at home can be very efficient in terms of the success of the rehabilitation, costs, and accessibility [100]. Consequently, there is interest in a device that can measure EMG and joint angle and is light and portable. While EMG measuring systems can be very portable (To record, the majority of these require at least a nearby computer), the gold standard for measuring movement is now considered marker-based optical motion capture technology. Thus this technique can be implemented only in the laboratory. As shown in Intoduction 1, inertial technology is a promising and increasingly popular approach to motion tracking outside the laboratory.

Cotton et al. device

Cotton et al. device uses MIMU and EMG technologies for rehabilitation [101].

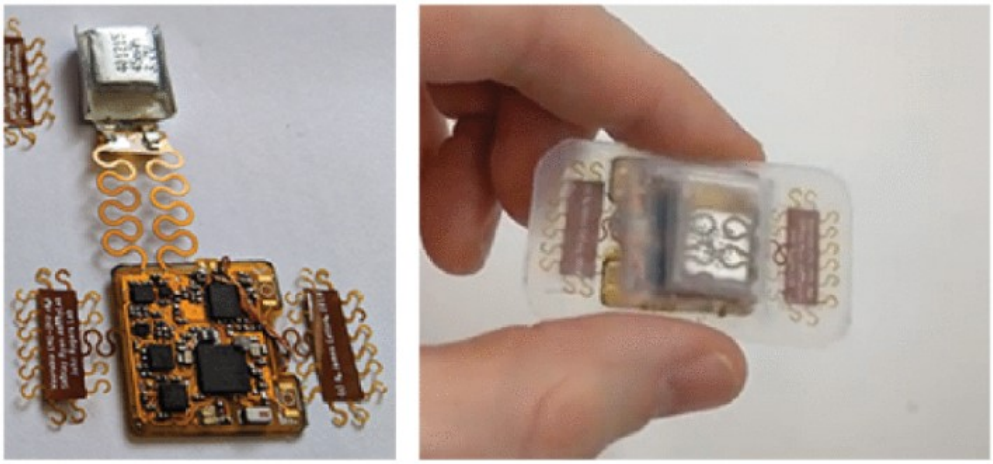

Figure 3.13: R. James Cotton and John Rogers's device [101]

They use a 9-axis MIMU sensor which records the acceleration, rotation, and magnetic data (MPU-9250, Invensense, San Jose, US), sampled at $500Hz$, with a maximum rotation rate at $500^{\cdot}/s$ and maximum acceleration of $16G$. A Bluetooth connection is implemented to send data to a smartphone. For orientation estimation, they used a Complementary filter. They evaluate the rotation angle multiplying quaternions obtained by the two MIMUs. This value is not the final angle; the sensors can be placed anywhere on the limbs, and this rotation must be considered.

This problem was solved by measuring the rotation in a natural pose and removing this baseline in the following measurement.

Trigno Avanti Sensor from Delsys

Trigno Avanti Sensor (Figure 3.14) is a commercial device that allows the acquisition of IMU and sEMG data in every environment. This device supports up to 16 channels for recording surface EMG signals. Each channel provides high-resolution EMG data for precise muscle activity measurement. It provides a high sampling rate of up to 2000 samples per second (Hz), allowing for capturing fast and detailed muscle activation patterns. In addition to EMG, the Trigno Avanti Sensor integrates triaxial inertial sensors to capture motion data. These sensors measure acceleration and angular velocity in three dimensions, providing valuable information about movement patterns. The sensor utilizes wireless technology for data transmission, enabling freedom of movement during data collection. It communicates wirelessly with the base station or receiver unit. The Trigno Avanti Sensor has a rechargeable battery, providing extended operating time and prolonged data collection sessions. Multiple Trigno Avanti Sensors can be synchronized to ensure accurate timing alignment between EMG and motion data, making it suitable for multi-channel and multi-segment analysis. Delsys provides proprietary software for data acquisition and analysis. The software offers real-time visualization, signal processing, and advanced analysis tools for interpreting EMG and motion data. The Trigno Avanti Sensor is compatible with other Delsys systems, such as force plates and motion capture systems, allowing for integrated measurement and analysis of multiple physiological parameters.

It has the dimensions of $27 \times 37 \times 13mm$ and weighs $14g$. It provides users with selectable angle data representations such as quaternion or Euler angles.

Figure 3.14: Trigno Avanti Sensor from Delsys

PicoX from Cometa

PicoX (Figure 3.15) is the new design from Cometa. They include a MIMU at a $500Hz$ sampling frequency that can be used by itself or combined with EMG. It can be made up of up to 36 synchronized channels. Its dimension and weight are, respectively, $41 \times 23 \times 14mm$, and $9.5gr$

EMG Sensor Channels: The PicoX system supports up to 16 channels for recording surface EMG signals. This number allows for capturing muscle activity from multiple muscles simultaneously.

The system offers a high sampling rate of up to 4000 samples per second (Hz), enabling precise and detailed measurement of muscle activation patterns.

To capture motion data, the PicoX system integrates inertial sensors, including accelerometers and gyroscopes. These sensors measure acceleration and angular velocity, providing information about movement patterns and orientation.

It utilizes wireless technology for data transmission, allowing for freedom of movement during data collection. It communicates wirelessly with the base station or receiver unit.

The PicoX system has a rechargeable battery that provides extended operating time for prolonged data collection sessions.

Multiple PicoX systems can be synchronized for precise timing alignment between EMG and motion data, facilitating multi-channel and multi-segment analysis.

Comet provides dedicated software for data acquisition and analysis. The software offers real-time visualization, signal processing capabilities, and advanced analysis tools for interpreting EMG and motion data.

The PicoX system is designed to be compatible with other Comet devices, such as force plates and motion capture systems, allowing for integrated measurement and analysis of various physiological parameters.

Figure 3.15: PicoX Sensor from Cometa

Myo Armband Sensor from North Inc.

Myo Armband (Figure 3.16) is a wearable device from Thalmic Labs (now part of North Inc.). It measures electrical signals from forearm muscles (EMG) and combines them with inertial sensors (gyroscopes and accelerometers) to track hand and arm gestures. His technical Specifications are:

- EMG Sampling Rate: 200 Hz
- IMU Sensor: 9-axis (3-axis accelerometer, 3-axis gyroscope, 3-axis magnetometer)
- Connectivity: Bluetooth
- Compatible Platforms: Windows, macOS, iOS, Android

The Myo Armband is designed to measure and interpret electrical signals produced by muscles, enabling gesture recognition and control based on muscle activity.

The armband features eight high-resolution EMG sensors strategically placed to capture muscle signals from the forearm.

In addition to EMG, the armband incorporates a 9-axis inertial measurement unit (IMU) consisting of an accelerometer, gyroscope, and magnetometer. These sensors provide information about arm movements, orientation, and motion tracking.

The Myo Armband utilizes Bluetooth technology to wirelessly connect to compatible devices such as computers, smartphones, or tablets, allowing real-time data streaming and control.

The armband has a rechargeable battery that provides several hours of continuous usage. The battery can be charged via a USB connection.

It employs sophisticated algorithms to interpret the sensors' muscle signals and motion data, enabling gesture recognition and control of compatible devices and applications.

North Inc. provides a Software Development Kit (SDK) that allows developers to create custom applications and integrations with the Myo Armband. The SDK includes programming libraries, documentation, and sample code to facilitate development.

The Myo Armband is compatible with various platforms, including Windows, macOS, iOS, and Android, making it versatile for integrating different applications and systems.

Figure 3.16: Myo Armband Sensor from North Inc.

Noraxon EMG Systems from Noraxon USA Inc.

Noraxon is a well-known EMG system manufacturer for capturing and analyzing muscle activity. Their EMG systems are widely used in research, clinical, and sports performance settings. This device provides synchronized data acquisition and analysis of muscle activity and motion Figure 3.17. Noraxon offers a range of EMG systems tailored for different applications and user requirements. They provide options for wired and wireless EMG systems and come in various channel configurations, allowing for simultaneous measurement of muscle activity from multiple sites. The number of channels can vary based on the specific system model and configuration, ranging from a few channels to systems capable of capturing data from dozens of channels. Their software allows real-time visualization of EMG signals, signal processing, and advanced analysis features for extracting relevant information from the recorded data. Noraxon EMG systems can be integrated with inertial sensors to analyze muscle activity and movement patterns comprehensively. Noraxon inertial sensors are typically designed to operate wirelessly, allowing for greater freedom of movement during data capture. They offer high sampling rates, allowing for precise capture of fast movements and dynamic motion patterns. The specific sampling rate may vary depending on the sensor model and configuration.

Figure 3.17: Noraxon EMG Systems from Noraxon USA Inc.

BTS FREEEMG from BTS bioengineering:

The BTS FREEEMG system integrates high-density EMG sensors and inertial sensors for advanced motion analysis. The BTS FREEEMG system utilizes high-density surface EMG sensors and supports up to 16 channels for capturing surface EMG signals simultaneously. It offers a high sampling rate for EMG data acquisition, typically ranging from 1000 to 2048 samples per second (Hz). The system combines EMG measurements with triaxial inertial sensors for motion analysis. It can integrate data from up to 4 inertial sensors placed on different body segments. The system employs wireless communication between the EMG sensors and the data acquisition unit, allowing for freedom of movement during data collection. The BTS FREEEMG system is compatible with other BTS systems, enabling integration with force platforms, gait analysis systems, and other physiological measurement devices.

Figure 3.18: BTS FREEEMG from BTS bioengineering

3.4.2 Acquisition device

The device, developed by Rossi et al. with the dimensions of $57.8mm \times 25.2mm \times 22.1mm$, was designed to acquire sEMG data [102].

It mounts an AmbiqMicro Apollo3 Blue as the MCU. It has a RAM availability of $384kB$ and fits into a $20.25mm^2$ space, with low current absorption requirements of $6\mu AMHz$ for the CPU (running up to $48MHz$) and $3mATX$ power transmitting at $0dB$.

Furthermore, an LSM6DSO32 imu sensor is implemented with a high-performance 3-axis digital accelerometer and 3-axis digital gyroscope. A 1.8 V constant voltage powers the circuitry of the entire unit.

Figure 3.19: Acquisition device, by Rossi et al. [102]

3.4.3 Encoder

The encoder used in this thesis work is an AMT20 compact modular package with a locking hub for easy installation. It features patented capacitive ASIC technology, low power consumption, and Serial Peripheral Interface (SPI) configurable settings. The encoder provides a 12-bit absolute position via SPI (4096 positions) and offers incremental resolutions up to 1024 PPR. It also includes an index pulse and operates within a wide temperature range of $-40 \sim 125°C$.

A simple code is used to interface with the encoder. The code provides functionality to set the zero position (representing the angle at which the device is initially positioned), read the position and timestamp, and handle start and stop commands.

Figure 3.20: AMT20 Encoder

Chapter 4

System description

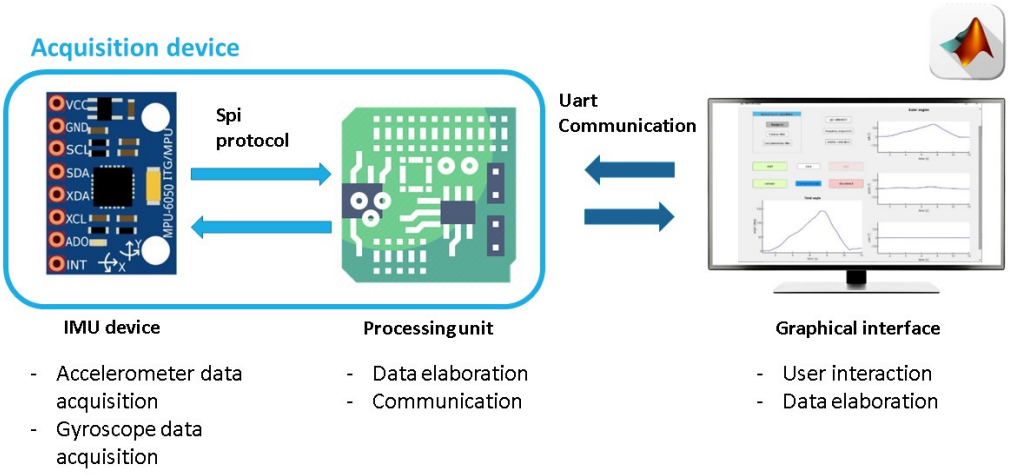

Figure 4.1: System overview

The system developed for this thesis work comprises two acquisition devices, each made up of an AmbiqMicro Apollo3 Blue microcontroller and an LSM6DSO32 IMU sensor (see Chapter 3 for more details), and an encoder. In order to visualize graphical outcomes and communicate with the devices, a Graphical User Interface (GUI) is developed using MATLAB.

The firmware of the IMUs encompasses various components such as SPI communication, UART interface, and the main function responsible for processing the sensor

measurements. Additionally, a calibration procedure is incorporated to account for any sensor inaccuracies and biases, enhancing overall system performance.

The GUI is an interactive platform that facilitates user interaction and control over the system. It provides a user-friendly interface for configuring settings, initiating data acquisition, and visualizing real-time sensor data. Users can easily monitor the joint angles through the GUI and access essential system parameters. A comprehensive validation protocol has been established to validate the system's accuracy and reliability. This protocol includes a series of controlled experiments and comparisons with reference measurements (the absolute encoder presented in the "State of Art chapter") to assess the system's performance under different conditions.

4.1 Firmware

The device's firmware incorporates several crucial components and functionalities to facilitate its operation. These include Serial Peripheral Interface (SPI) communication for efficient data exchange, a data acquisition module for capturing sensor data, a Universal Asynchronous Receiver Transmitter (UART) interface for external communication, a sensor calibration module for accurate measurements, and a main function module to oversee the overall operation of the device. The firmware's role is essential in enabling the seamless integration and functionality of the device in various applications.

4.1.1 Spi communication

An SPI interface enabled communication between the AmbiqMicro Apollo3 Blue microcontroller and the LSM6DSO32 IMU sensor. The access to the IMU (slave) registers is based on read-and-write transactions between the microcontroller (master) and the sensor.

Read and write register commands are completed in 16 clock pulses or multiples of 8 in the case of multiple read/write bytes. SPI communication utilizes a 4-wire connection: Master Input Slave Output (MISO), Master Output Slave Input (MOSI), Serial Clock (SCK), and Chip Select (CS).

The Chip Select (CS) line, controlled by the SPI master, enables the serial port. The Serial Clock (SCK), also controlled by the SPI master, provides the clock signal for synchronous communication. MISO and MOSI are responsible for the serial output and input data, respectively, between the LSM6DSO32 IMU and the microcontroller.

Communication begins with a Read/Write bit (RW). If this bit is set to 0, 7 bits of Data In (DI(7:0)) are written into the device. If set to 1, 7 bits of Data Out (DO(7:0)) are read from the output serial port.

An additional 6 bits are available in the input serial interface of the IMU after the RW bit. These represent the address field of the indexed register. In the case of multiple read commands, a period of 8 clocks is added, and the address is increased for each block.

The SPI interface was implemented in mode 0, where the Clock Polarity (CPOL) and Clock Phase (CPHA) are set to 0. In this mode, the clock is idle at 0, and the SPI data is sampled at the leading edge of the clock signal. Please refer to Figure 4.2 for a visual representation of SPI communication in mode 0.

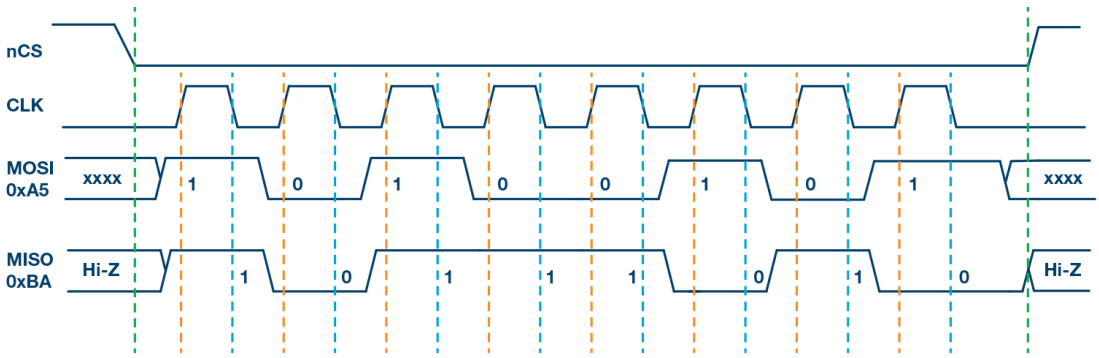

Figure 4.2: SPI communication 0 mode [103]

4.1.2 Data acquisition

Accelerometer and gyroscope data are stored in six registers containing the most significant and least significant parts of the acceleration and gyroscope signals along the X, Y, and Z axes. Each axis's complete data is represented by a 16-bit number obtained by concatenating the most significant and least significant parts. All values are encoded as two's complement numbers.

The accelerometer has a full scale of $\pm 4g$, indicating that it can measure accelerations within a range of ± 4 times the acceleration due to gravity. On the other hand, the gyroscope has a full scale of ± 250 degrees per second (dps), indicating its measurement range for angular velocity.

The timestamp data comprises four registers, resulting in a 32-bit unsigned number. This value represents the time the data was acquired and can be used for synchronization or time-based analysis.

Different strategies can be employed to determine when the data is ready to be read. One approach is to monitor the status register, which provides information about the availability of new data. Alternatively, an interrupt mechanism can be utilized, where the sensor triggers an interrupt signal when new data is available. Lastly, a First-In-First-Out(FIFO) buffer can store several data samples, allowing batch processing or reducing the data read frequency.

Three methods (status register, interrupt, and FIFO) were tested and evaluated to determine the most suitable strategy for our requirements. The evaluation aimed to identify the best performance, efficiency, and reliability approach for our intended purpose.

Status register

The LSM6DSO32 sensor incorporates a status register that plays a crucial role in determining the availability of new data. By checking the status register, it is possible to determine whether a new data set is ready for retrieval and processing.

Two specific bits, XLDA and GDA, are of interest within the status register. The XLDA bit indicates the availability of new data from the accelerometer, while the GDA bit signifies that data from the gyroscope is ready to be read. When XLDA equals 1, the accelerometer produces a new data set. When GDA equals 1, the gyroscope data is available for retrieval.

An algorithm was implemented to exploit this register and determine the availability of data. While not the most efficient solution, it provides a straightforward approach to data acquisition. The algorithm begins by checking the status register to see if the XLDA or GDA bit is set to 1, indicating the availability of new data. If data is indeed available, the algorithm proceeds to acquire and process the data.

Following data acquisition, the algorithm incorporates a 2-second delay before rechecking the status register. This delay maintains a data acquisition frequency of 100Hz, a commonly used frequency in sensor fusion algorithms found in the literature [104]. By adhering to this frequency, the algorithm ensures that data is acquired regularly, allowing for accurate sensor fusion and subsequent analysis.

Interrupt-based acquisition

Interrupts in the LSM6DSO32 are exclusively generated by the accelerometer and are triggered based on the accelerometer status register. This register plays a crucial role in determining the availability of fresh sensor data. When the value of the accelerometer status register is set to 1, an interrupt signal is sent by the LSM6DSO32 sensors, indicating that a new data set is ready for acquisition. This interrupt-driven approach ensures efficient and timely data retrieval from the accelerometer.

The system's sensor frequency for the accelerometer was set to 104 Hz. This frequency setting dictates the rate at which sensor measurements are acquired and processed. The system can maintain a consistent data acquisition rate by aligning the interrupt-based data acquisition with this frequency, enabling reliable motion tracking and analysis. This chosen frequency of 104 Hz is commonly utilized in sensor fusion algorithms and is widely documented in the literature [104].

Fifo acquisition

Including a FIFO (First-In-First-Out) buffer in the LSM6DSO32 sensor brings significant advantages to the system's power management. By utilizing the FIFO, the host processor no longer needs to poll the sensor for data continuously. Instead, it can remain in a low-power state and selectively wake up when necessary to retrieve a burst of data from the FIFO. This approach ensures consistent power savings for the overall system.

The LSM6DSO32 FIFO has a storage capacity of up to 3 kilobytes of data (or 9 kilobytes if the data are compressed). It can accommodate data from various sources, including the gyroscope, accelerometer, external sensors (up to 4), step counter, timestamp, and temperature. In our specific configuration, we only store data from the accelerometer, the gyroscope, and the timestamp.

The process of writing data to the FIFO is triggered by the data-ready signal, indicating that new sensor measurements are available for storage. We set a threshold of 39 samples in the FIFO to optimize the data acquisition process. Considering the sampling rate of the sensors set to 104 Hz, this threshold allows us to capture a signal length of 130 milliseconds.

Data stored in the FIFO are organized in dedicated registers. Each FIFO word consists of 7 bytes, comprising one tag byte identifying the sensor source and 6 bytes of fixed data. It is important to note that the tag byte also includes a parity bit, which serves as a checksum to detect any corruption in the content of the output register. As with the previous data acquisition system, once the data and parity bit are obtained from the FIFO, they undergo further processing and analysis. However, in this case, the data elaboration process becomes slightly more complex due to the additional step of checking the parity bit for data integrity.

Comparison

As shown in Figure 4.3, the data acquisition frequency is nearly identical among the three methods. However, factors other than frequency were considered when selecting the best implementation for our device. Although functional, the manual check of the data-ready register is not the most flexible solution, as the frequency is determined by the delay time, which lacks rigor. Therefore, this technique was discarded. Both the interrupt method and FIFO mode offer controlled frequency acquisition changes. However, after consulting the datasheet, we discovered that the FIFO mode is the lightest solution, aligning with our goal of keeping the system as lightweight as possible. Hence, we decided to implement the FIFO mode in the final device.

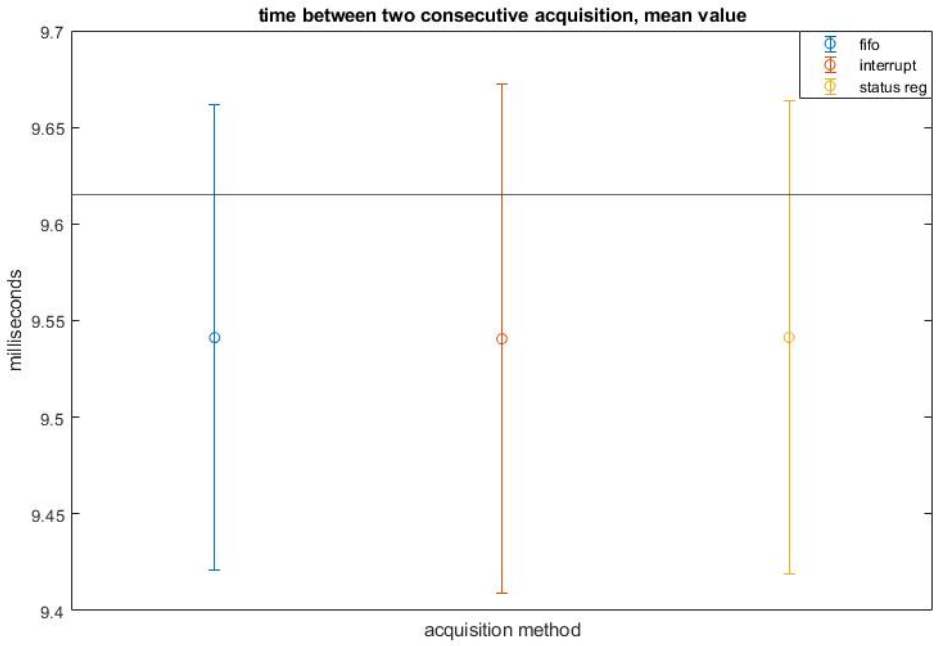

Figure 4.3: time mean values and sdv for three acquisition systems: status register, interrupt and fifo

4.1.3 UART interface

A UART enables communication between the microcontroller and the computer through a wired connection. It facilitates two types of transactions: one for reading data from the microcontroller and another for writing data to the microcontroller.

In the device, UART functionality was implemented with specific characteristics:

1. The baud rate, which determines the transmission speed, was fixed at 460800 bits per second.
2. Parity was not checked during data transmission. Parity is a method of error checking that can be used to ensure data integrity.
3. The data size for each transmission was set to 8 bits. 8 bits of data are sent or received in each transaction.
4. One stop bit was used to indicate the end of each data transmission.

Additionally, a UART interrupt was implemented in the microcontroller. This interrupt is triggered when the microcontroller receives data from the computer, allowing the microcontroller to respond to the received data promptly.

UART Commands

The microcontroller can initiate different operations based on the strings received through the UART interface. When the "*start*" string is received, the microcontroller initializes all the sensors. Upon receiving the "*gyr_calibration*" string, the microcontroller obtains 4000 samples for calibrating the gyroscope sensor. This calibration procedure must be performed before starting data acquisition. If the "*stop*" string is received, the IMU is reset.

The commands "*madgwick*", "*kalman_filter*", and "*complementary_filter*" are used to select the sensor fusion algorithm for data processing.

4.1.4 Sensors calibration

For sensor calibration, the procedure proposed by Stančin et al. was followed due to its efficiency in terms of time and computational complexity and because it does not require additional equipment [105].

Accelerometer

Accelerometer calibration should be performed whenever there is a significant change in the sensor's operating temperature. The calibration is based on the principle that the sensor, if not applied any force, should display a $1g$ acceleration along the

axis normal to the horizontal surface and $0g$ along the other axis. Measurements are taken in six different orientations while the sensor rests on an even horizontal surface. These measurements are divided into two triplets: one consisting of all the values with positive acceleration and the other with negative values, as shown in Figure 4.4.

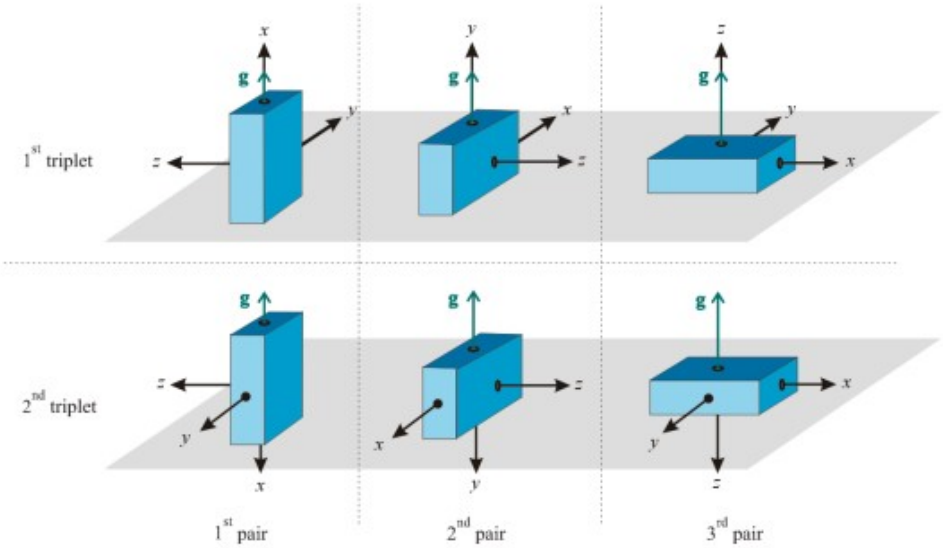

Figure 4.4: Acquisition sequence for Accelerometer calibration [105]

The obtained measurements are then used to form two matrices, A_{s+} and A_{s-}, which concatenate three vectors representing the mean values of the accelerometer acquisition's x, y, and z components. In A_{s+}, the first vector corresponds to the accelerometer's x-axis aligned with gravity, the second vector corresponds to the y-axis aligned with gravity, and the third vector corresponds to the z-axis aligned with gravity. Similarly, the A_{s-} matrix is obtained by aligning the accelerometer axis with $-g$.

Using these matrices, a calibration matrix, C_s, and a zero-level offset vector, A_0, are calculated as follows:

$$C_s = 2(A_{s+} - A_{s-})^{-1} \tag{4.1}$$

$$A_0 = \frac{A_{s+} + A_{s-}}{2} \tag{4.2}$$

$$a_0 = \frac{A_0 \cdot i}{3} \tag{4.3}$$

where i is a 3×1 vector of ones.

Once these coefficients are obtained, the calibrated accelerometer values, a, can be easily calculated using Equation 4.4:

$$a = C_s \cdot (a_s - a_0) \tag{4.4}$$

where a represents the calibrated accelerometer values and a_s represents the accelerometer values from the sensor.

After performing the accelerometer calibration procedure, significant improvements in data quality were observed (Figure: 4.5). The calibrated data aligned better with the expected 0 and 9.8 m/s² values. Before calibration, the raw accelerometer readings showed slight deviations from these reference values. However, after applying the calibration parameters derived from the calibration procedure, the data became more closely aligned to 0 when no acceleration was present and to 9.8 m/s² under the influence of gravity. This improved alignment indicates that the calibration process effectively reduced biases and errors in the accelerometer measurements.

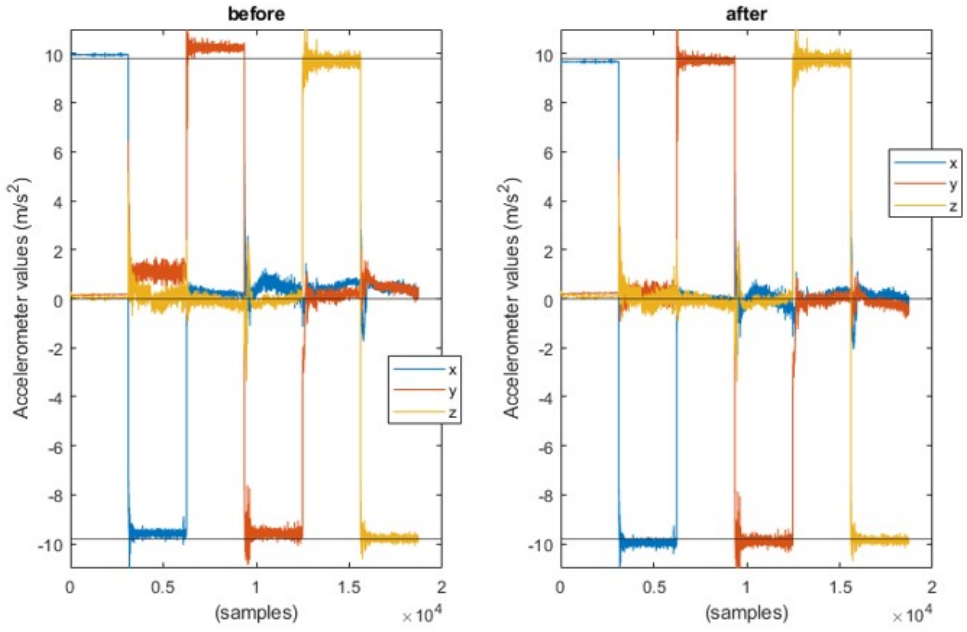

Figure 4.5: Acclerometer values in each direction before and after the calibration

Gyroscope

The gyroscope calibration procedure needs to be performed each time the sensor is turned on since the bias from this sensor is one of the primary sources of noise in IMU acquisition. A simple calibration approach involves subtracting an offset

value from the gyroscope values obtained from a static acquisition along the three axes. A more complex calibration method is proposed in [105], but it cannot be fully implemented in our system due to the presence of cables in the hardware configuration.

Despite the simplicity of our calibration approach, it has proven to be highly efficient in improving the accuracy and reliability of the gyroscope measurements. Figure 4.6 visually demonstrates the impact of the calibration process by comparing the gyroscope's integrated values before and after calibration. Before calibration, the gyroscope readings exhibited slight drift and systematic errors, resulting in cumulative inaccuracies over time. However, after applying the calibration procedure, the gyroscope's integrated values showed significant improvement, with reduced drift and better alignment with the expected values. This calibration process mitigated biases and errors, resulting in more precise and reliable angular velocity measurements.

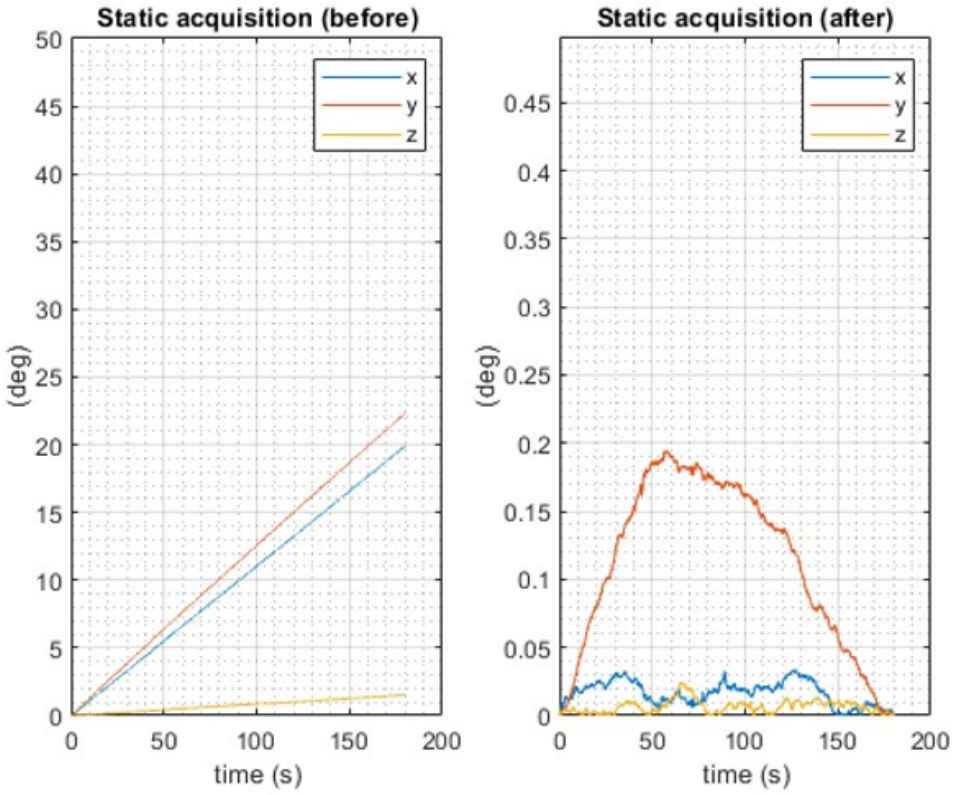

Figure 4.6: Gyroscope values integrated in each direction before and after the calibration

4.1.5 Main function

The main function is the entry point of the program, where the execution of the code begins. In this particular code, the main function configures and initializes various peripherals and devices for SPI communication between the microcontroller and the slave sensor.

The code begins by including the necessary header files for the microcontroller, BSP (Board Support Package), standard input/output, utility functions, device drivers, sensor fusion operations library, and sensor fusion library. It also defines several constants and variables required for SPI communication and data processing.

Next, the code defines the UART configuration, as the UART is used for communication and debugging purposes. It sets the baud rate, data bits, parity, stop bits, and flow control for the UART. It also configures the UART buffers and initializes the UART interrupt.

After configuring the UART, the code sets up the SPI communication. It initializes the SPI interface and configures the SPI parameters, such as clock frequency and mode. It also configures the GPIO pins for SPI communication.

The code then configures the interrupt for the GPIO pin that receives interrupts from the slave sensor. It registers a callback function to handle the interrupt and enables the GPIO interrupt.

Next, the code initializes the SPI handle and configures the SPI transactions for reading and writing data to the slave sensor. The SPI transactions include instructions, direction, buffer sizes, and chip select information.

Once the configurations are complete, the main function enters an infinite loop. Inside the loop, it waits for the *data_ready* flag to be set, indicating that new data is available from the slave sensor. When the flag is set, the main function reads the data from the sensor using SPI transactions and processes the received data.

Data Elaboration

Once the data is acquired, the accelerometer data is converted to g units, and the gyroscope data is converted to rad/sec.

Calibration coefficients, previously calculated, are applied to the sensor and timestamp values.

The timestamp data is converted to *seconds* using the conversion factor:

$$ConversionFactor = 40000 \cdot (1 + 0.0015 \cdot freqfine) \tag{4.5}$$

Here, $freqfine$ represents the actual timestamp resolution obtained from the INTERNAL FREQ FINE register.

Three different sensor fusion algorithms are then used to determine the 3D orientation of the device: the Extended Complementary Filter [106], the Madgwick

algorithm [34], and the Extended Kalman filter [107]. A more detailed explanation of these algorithms can be found in the "Introduction" chapter (1).

Once the data is elaborated, it is sent through the UART interface in the following sequence: timestamp (*seconds*), gyroscope values (*dps*), accelerometer values (g), and quaternion values.

4.2 GUI

As shown in Figure 4.7, a graphical interface is implemented in MATLAB programming language. It enables the user to send commands to the microcontrollers and acquire data from two IMUs to calculate the relative angle between the devices.

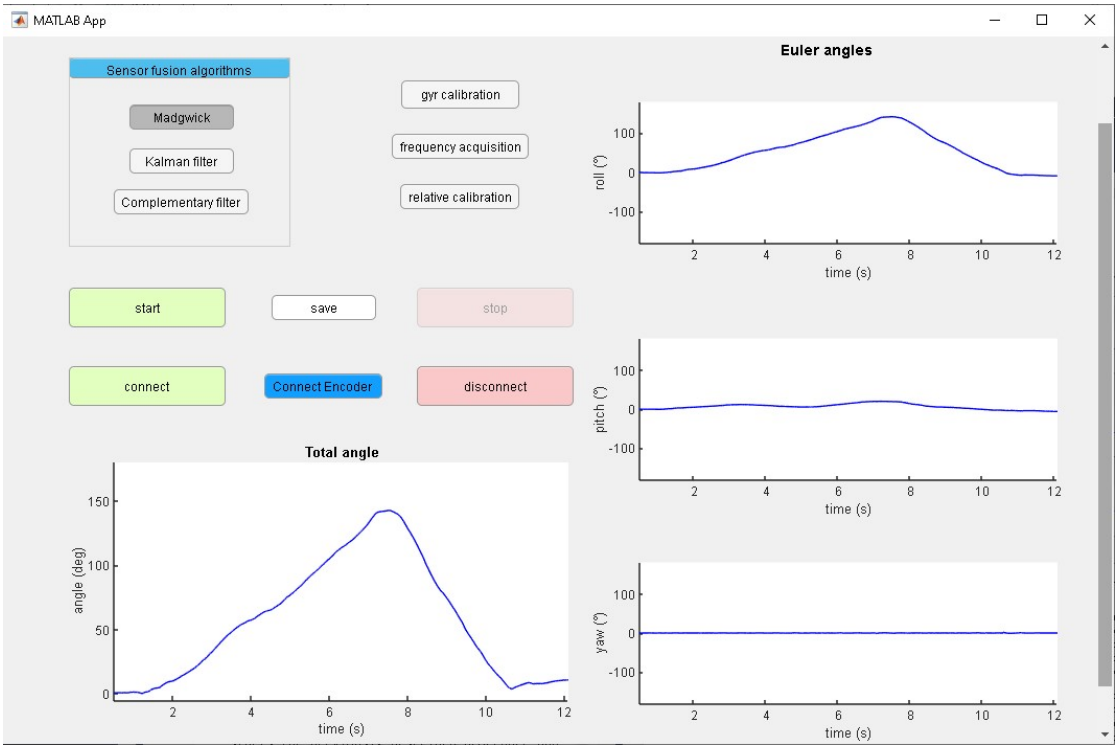

Figure 4.7: Graphical interface implemented in MATLAB programming language

The interface consists of the following components:

Connect button

This button establishes the connection between the IMUs and the serial port.

Connect encoder

When this button is pushed, it enables the connection of the encoder to the serial port.

Gyr calibration button

Pressing this button initiates the gyroscope sensor calibration. The program sends a "*gyr*" command through the UART interface, and the microcontroller starts the calibration procedure to obtain new gyroscope sensor calibration coefficients. The LED on the device toggles upon completion of this procedure.

Sensor fusion algorithms button group

The user can choose the desired algorithm for data processing. This selection should be made before starting data acquisition.

Relative Angle Plot

This plot displays the three components of the Euler angles. The x-axis represents time in seconds, and the y-axis represents the angle value in degrees.

Angle plot

This plot shows the total angle of rotation. The x-axis represents time in seconds, and the y-axis represents the angle value in degrees.

Frequency acquisition button

When pressed, the acquisition devices send data to the computer, allowing the program to acquire 5 seconds of timestamp data and compute the mean difference of the values. This procedure determines the real acquisition devices' sampling rate. Finally, a "stop" command is sent to the microcontroller, the LED is set to a fixed state, and all variables are cleared.

Relative calibration button

Pressing this button computes the initial angle between the acquisition devices, which needs to be subtracted from the final angle. The computer sends the selected sensor fusion algorithm's string and a start command to the microcontroller to initiate the calibration procedure. The algorithm begins acquiring data from both the acquisition devices, storing quaternion and timestamp values in buffers. Once both IMU buffers contain at least one data point, the time buffers are converted

into sample buffers using the previously computed frequency. To synchronize the data from the two IMUs, further processing is performed only on quaternion values corresponding to the same sample value. The relative quaternion is obtained as the product of the quaternion from one acquisition device with the inverse of the quaternion from the other. The relative angle is two times the arccos of the scalar part of the relative quaternion, which is then converted to degrees. The relative quaternions are also converted to Euler angles for better visualization by the user. The offset is determined as the mean value of the relative angle over a 30-second acquisition. After 30 seconds, all variables are cleared.

Start button

When the Start button is pressed, the program sends a command string to the microcontroller containing the selected algorithm command and a start command. A start message is also sent to the encoder if it is connected. Data acquisition from the IMUs begins. Once data is available from both IMUs, the program performs data elaboration. It checks the data synchronization using the timestamp values, considering a maximum misalignment based on the acquisition device period. The joint quaternion is computed by multiplying the quaternion from one IMU with the inverse quaternion from the other IMU. The program analyzes $0.5s$ windows and determines if there are no movements based on gyroscope values to correct for yaw angle drift (caused by the characteristic of the gyroscope sensor). If no movements are detected, the program computes the coefficients of a rectification function. If movements are present, the coefficients are not updated. The rectification function is then subtracted from the previous quaternion.

The corrected quaternion is then converted to an angle in degrees as the double of the *arcos* function of the real part of the quaternion, and the plots are updated. The plots are refreshed every $0.5s$, showing a $20s$ real-time observation.

Figure 4.8 and Figure 4.9 illustrates the effectiveness of the dedrift process, showcasing the total angle data and the yaw angle data before and after dedrift. It is evident from the figure that the applied procedure, even if it is a simple procedure, successfully mitigates yaw angle drift and improves the system's accuracy.

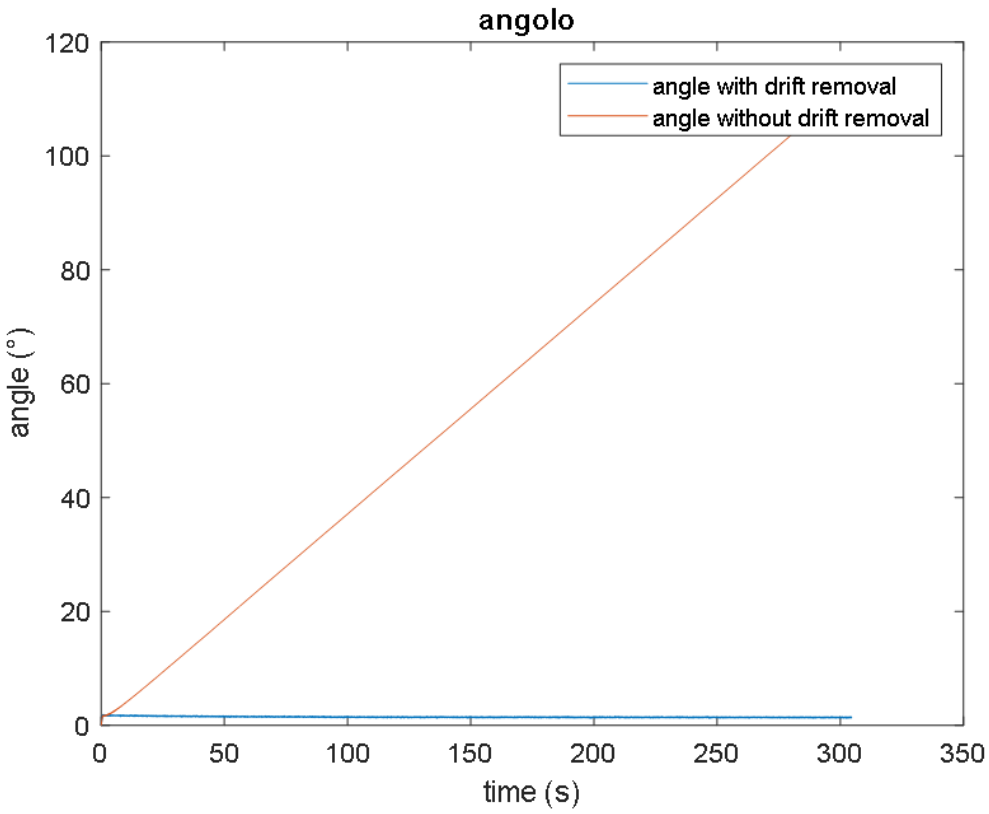

Figure 4.8: Total angle before and after linear detrend, 5min acquisition

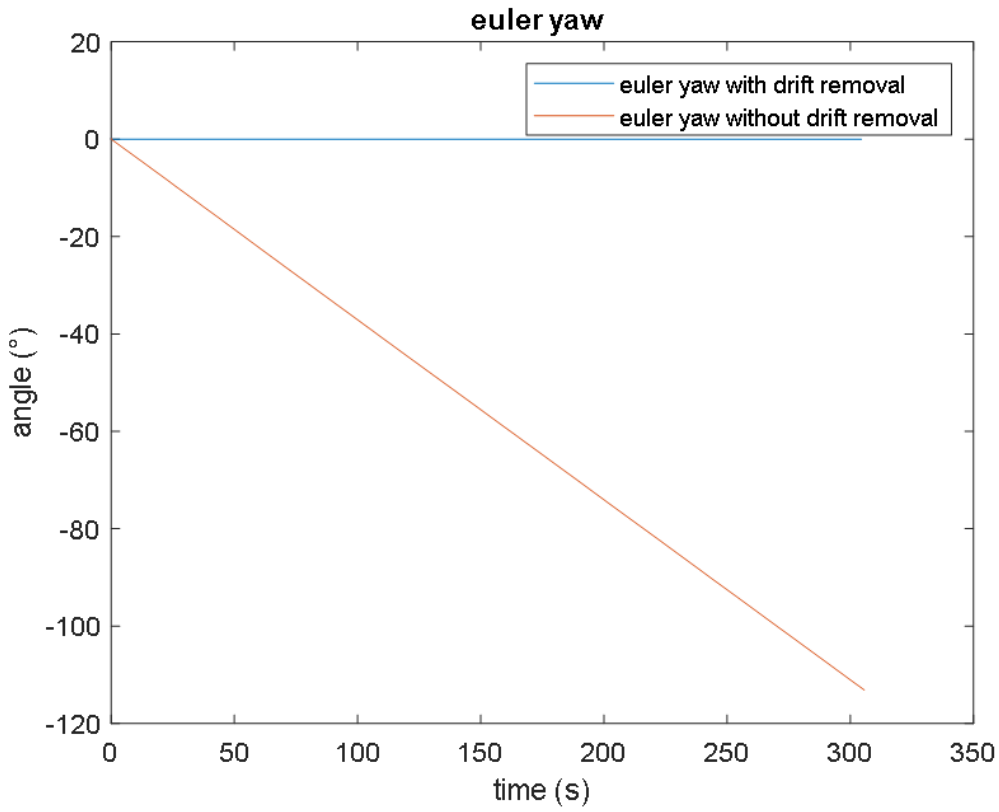

Figure 4.9: IMU Yaw angle before and after linear detrend, 5min acquisition

Stop button

Pressing this button sends a "stop" command through the UART to the microcontroller, stopping the data transmission and toggling the LED.

Save button

When pressed, it saves data stored in the following matrices:

- imuAngacquisition_[time]: This matrix contains the accelerometer and gyroscope data from both IMUs, along with the corresponding quaternion and timestamp values.
- jointAngacquisition_[time]: This matrix includes the timestamp values, total angleSequence, and total eulerSequence.
- Encoderacquisition_[time] (if encoder connected): This matrix contains time and angle values acquired from the encoder.

The [time] represents the time of acquisition expressed as d-MMM-y_HH-mm-ss ("d" - Day of the month as a decimal number (1-31), "MMM" - Month as an abbreviated name (e.g., Jan, Feb, Mar), "y" - Year without century (0-99), "HH" - Hour in 24-hour format (0-23), "mm" - Minute (00-59), "ss" - Second (00-59)).

Disconnect button

This button disables the connection with USB ports.

4.3 Validation protocol

The validation protocol aims to scientifically evaluate the performance and accuracy of the proposed acquisition devices for measuring arm flexion-extension movements. The validation will be conducted using a digital encoder as the reference standard. This protocol provides a comprehensive and rigorous procedure for conducting the validation study.

4.3.1 Validation Steps

Gyroscope Calibration

The sensors are calibrated using the previously described calibration procedures to minimize errors and biases, ensuring accurate measurements during data acquisition.

Computation of Relative Device Positions

The relative positions of the acquisition devices are calculated to determine their spatial relationship. Accurate spatial information is essential for the precise computation of arm flexion-extension angles.

Device Placement

The acquisition devices are positioned on the subject's arm in two different configurations:

1. Configuration 1 (Figure 4.10 A): The devices are placed near the elbow and shoulder, away from the muscles, aiming to minimize errors linked to the rotation of the hand and mitigate the effects of muscle interference on arm flexion-extension angle computation.

   In this configuration, the devices are positioned strategically to ensure accurate measurement of arm movements. Placing the devices near the elbow and shoulder helps minimize errors associated with hand rotation. This is crucial

as the rotation can introduce deviations in the computed flexion-extension angles.

Additionally, positioning the devices away from the muscles reduces the influence of muscle interference on the measurement. Muscles surrounding the arm can generate unwanted noise that might affect the accuracy of the acquired data. Placing the devices away from muscle regions minimizes the potential for signal contamination from muscular activity, resulting in more reliable measurements of arm flexion-extension angles.

While the literature does not provide a definitive consensus on the optimal IMU position for acquiring arm angle measurements [108], this particular configuration has been identified as one of the most accurate approaches for measuring arm flexion-extension angles [109].

2. Configuration 2 (Figure 4.10 B): The devices are placed on the biceps and forearm muscles, taking into consideration their future integration with an electromyography (EMG) acquisition system. One device is positioned on the biceps muscle and the other on the forearm muscles, following the placement recommendations outlined in the literature for EMG acquisition systems.

   The first device is attached to the biceps muscle, on the belly muscles, located on the anterior side of the upper arm. This placement allows for optimal measurement of muscle activity in the biceps during arm movements. The device is securely fastened to ensure reliable data acquisition from the biceps muscle [110].

   The second device is positioned on the forearm muscles, encompassing various muscles responsible for forearm movements. Placing the device on the forearm muscles enables precise monitoring of muscle activity in this region during arm flexion-extension tasks. Like the first device, proper attachment is ensured to maintain consistent data collection from the forearm muscles [111].

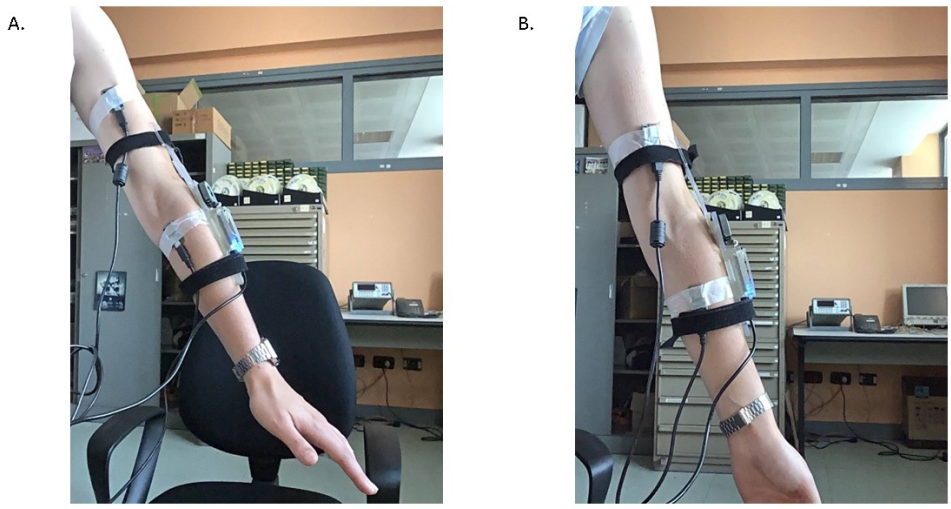

Figure 4.10: A. Acquisition Device Configuration 1, B. Acquisition Device Configuration 2

Arm Inclination

The system's performance is evaluated under different arm postures, specifically at 45° (Figure 4.11 A) and 90° (Figure 4.11 B) inclination relative to the body.

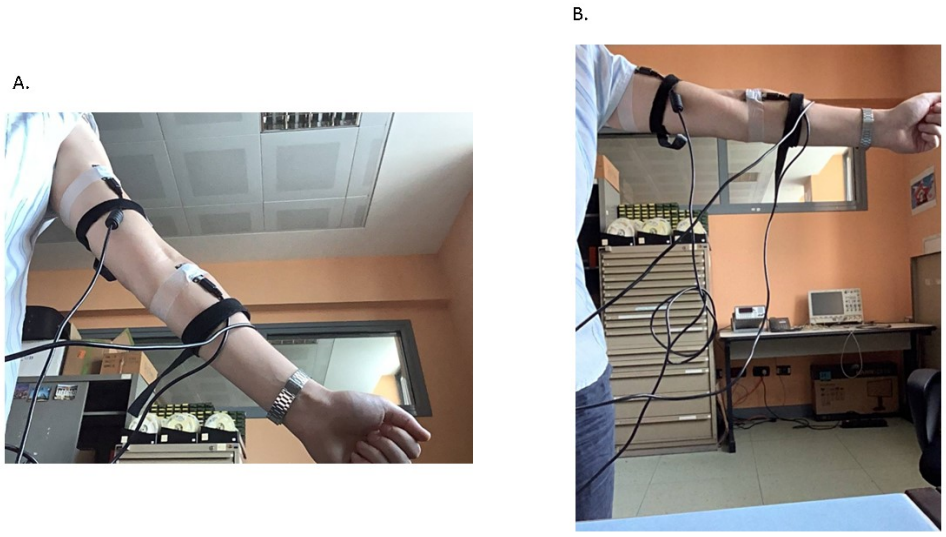

Figure 4.11: A. 45° Configuration, B. 90° Configuration

Encoder Placement

The digital encoder is positioned on the subject's arm, aligning its arms with the joint segment of the subject's arm. The encoder serves as the reference standard for measuring arm flexion-extension angles.

4.3.2 Data Elaboration Steps

Subject Instructions

Clear instructions are provided to each subject to perform a sequence of arm flexion-extension movements at different velocities, interspersed with rest periods:

1. Rest: Begin with a 10-second rest period to establish a baseline.
2. Movements: Perform 10 consecutive arm flexion-extension movements at a mean velocity (computed as the norm of the gyroscope of the forearm device) of $37.284 \pm 1{,}429$ dps, followed by a 5-second rest period.
3. Movements: Perform 10 consecutive arm flexion-extension movements at a mean velocity of $42.746 \pm 2{,}161$ dps, followed by a 5-second rest period.
4. Movements: Perform 10 consecutive arm flexion-extension movements at a mean velocity of 104.234 ± 2.785 dps, followed by a 5-second rest period.

5. Data Saving: Save the acquired data for subsequent analysis.

The acquired data are then saved for subsequent analysis.

4.3.3 Data Analysis

Data Loading

Quaternion Extraction

Three sensor fusion algorithms (Madgwick, Kalman, and complementary filter) extract quaternions from the acquired data. The quaternion processing is performed in MATLAB to expedite the subject data acquisition process. This decision is based on a preliminary analysis that compares the quaternion results obtained from MATLAB and the device firmware.

A random movement is executed through the analysis, and the data are evaluated using firmware-based computations and MATLAB-based computations. The mean square error (MSE) is utilized to quantify the disparity between the results obtained from the two approaches. The MSE can be calculated using the following equation:

$$MSE = \frac{1}{n}\sum_{i=1}^{n}(x_i - y_i)^2$$

Here, x_i represents the values derived from the firmware-based computations, y_i represents the values obtained from the MATLAB-based computations, and n denotes the total number of data points analyzed.

The preliminary analysis reveals a mean square error on the order of, or less than 10^{-5} between the MATLAB-based computations and the firmware-based computations. This indicates a relatively small discrepancy, providing confidence in using MATLAB for quaternion processing. By leveraging MATLAB, the time required for subject data acquisition can significantly reduce while maintaining consistent and accurate results.

Yaw Detrend and Angle Computation

A detrending process is applied to eliminate yaw drift, which can introduce errors in the computed angles using the same methodology employed in the graphical user interface (GUI). This ensures consistency in angle calculation and facilitates reliable comparison.

Signal Segmentation

The data are segmented to isolate the segments corresponding to arm movement while excluding rest periods. Utilize MATLAB's "findpeaks" function to identify

the maximum and minimum points in the signal, considering the peaks occurring between the nearest minimums before and after each maximum. This segmentation allows for a focused analysis of movement-specific data.

Root Mean Square Error (RMSE) Calculation

The discrepancy between the measured angles from the acquisition devices and the corresponding angles obtained from the encoder is quantified using the RMSE. The RMSE is computed using the following equation:

$$\text{RMSE} = \sqrt{\frac{\sum_{i=1}^{N}(\text{angle}_{\text{acquisition}_i} - \text{angle}_{\text{encoder}_i})^2}{N}}$$

Chapter 5

Results

5.1 Validation Results

The validation study yielded quantitative results that assess the performance and accuracy of the proposed acquisition devices for measuring arm flexion-extension movements. The obtained data were analyzed using various configurations, velocities, and sensor fusion algorithms. The following section presents the key findings of the validation study.

Configuration	Algorithm	mean	std
S1:S7-V1-P1	V1-P1_complementary	11.23	4.74
	V1-P1_kalman	20.28	3.76
	V1-P1_madgwick	11.48	4.50
S1:S7-V2-P1	V2-P1_complementary	8.77	3.81
	V2-P1_kalman	16.00	2.78
	V2-P1_madgwick	9.11	3.78
S1:S7-V3-P1	V3-P1_complementary	8.05	2.34
	V3-P1_kalman	11.52	4.50
	V3-P1_madgwick	9.86	2.97
S1:S7-V2-P1-45	V2-P1-45_complementary	31.93	12.18
	V2-P1-45_kalman	34.37	13.48
	V2-P1-45_madgwick	31.88	12.24
S1:S7-V2-P1-90	V2-P1-90_complementary	47.42	8.05
	V2-P1-90_kalman	50.27	7.49
	V2-P1-90_madgwick	45.14	7.72
S1:S7-V1-P2	V1-P2_complementary	14.44	7.03
	V1-P2_kalman	22.87	8.03
	V1-P2_madgwick	17.04	8.28
S1:S7-V2-P2	V2-P2_complementary	10.24	6.91
	V2-P2_kalman	20.13	7.38
	V2-P2_madgwick	11.01	7.10
S1:S7-V3-P2	V3-P2_complementary	8.69	3.33
	V3-P2_kalman	13.53	2.66
	V3-P2_madgwick	10.89	3.76

In the table above, "P1" and "P2" represent Configuration 1 and 2, respectively. "V1," "V2," and "V3" correspond to the slowest, middle, and fastest velocities as described in 4. "Complementary", "kalman" and "madgwick" indicate the algorithms used for the RMSE calculations. Finally, "Mean Value" and "std" represents the mean value and standard deviation of the RMSE for each combination of configuration, velocity, and algorithm.

5.2 Algorithm Comparison: Size and Time

In our evaluation of the Madgwick, Kalman, and Complementary Filter algorithms, we analyze their performance and consider other crucial factors. One such factor is the size of the algorithms, which refers to the memory space they occupy. Additionally, we measure the time required for each algorithm to calculate the

quaternion. Lastly, we assess the battery consumption of these algorithms on the device.

Algorithm size

The size of an algorithm plays a vital role in resource-constrained environments. When comparing Madgwick, Kalman, and Complementary Filter, we observe that they have different sizes. The Madgwick algorithm requires a memory space of $19.99kB$, the Kalman algorithm requires $20.24kB$, and the Complementary Filter algorithm requires $19.84kB$. Evaluating the size can help us understand the feasibility of implementing these algorithms in various hardware and software configurations.

Algorithm Time

Another significant aspect to consider is the time each algorithm requires to obtain the quaternion. The Madgwick algorithm takes approximately $0.0639ms$, the Kalman algorithm takes around $0.3863ms$, and the Complementary Filter algorithm takes about $0.0471ms$. Understanding the time requirements of these algorithms is crucial for real-time applications where responsiveness and efficiency are crucial.

By considering the size and time of the Madgwick, Kalman, and Complementary Filter algorithms, we can comprehensively evaluate their performance and suitability for specific applications.

Chapter 6

Conclusion and future work

6.1 Conclusion

In conclusion, this thesis has presented a preliminary development of a motion tracking system based on IMU technology for comprehensive monitoring and assessment of movement execution during rehabilitation therapy. The primary objective of this study has been accomplished, providing initial insights into the system's performance and potential areas for improvement.

The obtained results align with existing literature, demonstrating lower error rates for Configuration 1, tath is the configuration accompanied and reported in literature work, and higher error rates for Position 2, which aligns with arm muscles.

We thought that slower movement would produce less error because, in this situation, the accelerometer is affected by less external acceleration, and the elaboration time of the sensor fusion algorithms will not result in the loss of significant samples. However, an unexpected finding emerged, revealing higher error rates for slow movements than for fast ones. This discrepancy may be attributed to the less fluid nature of slow movements, which introduced inconsistencies in the motion data.

The observed significant error rates at 45 and 90 degrees arm positions necessitate further investigation. A thorough analysis, coupled with experimental studies, is essential to understand the factors contributing to these elevated error rates and develop strategies to mitigate them. Addressing this issue can be achieved through improved relative calibration of initial conditions or by incorporating a magnetometer for enhanced accuracy.

Consistent with expectations, the comparative evaluation of fusion algorithms revealed that Madgwick and complementary filter algorithms outperformed the Kalman filter regarding execution time and memory usage. Consequently, these

algorithms exhibit promising potential for applications that emphasize real-time performance and resource efficiency.

It is crucial to emphasize that this work represents an early-stage exploration of the IMU-based motion tracking system. The ultimate goal is to integrate this system with an EMG acquisition system, although this integration remains an avenue for future research. Subsequent efforts will focus on refining the system, addressing the identified limitations, and integrating it seamlessly with an EMG acquisition system to deliver a comprehensive solution for monitoring and assessing patients during rehabilitation therapy.

In summary, this thesis has provided valuable insights into developing a motion-tracking system based on IMU technology. The results contribute to the existing body of knowledge, shedding light on the system's potential and delineating areas for further investigation and refinement. The findings lay the groundwork for future advancements and research endeavors in motion tracking and its integration with EMG acquisition for improved rehabilitation therapy outcomes.

6.2 Future Work

Several avenues for future work and improvement can be explored based on the findings of this thesis:

Refining Sensor Calibration: Further enhancing the relative calibration of the sensors can lead to increased accuracy and reliability in the IMU-based motion tracking system. Fine-tuning the calibration process and exploring advanced techniques may improve the overall performance.

Optimization of Sensor Fusion Algorithms: The sensor fusion algorithms can be optimized by refining the coefficients and parameters used for data fusion. Investigating advanced algorithms or modifications to the existing ones may lead to improved estimation of body orientation and movement.

Yaw Detrend Improvement: The absence of a magnetometer can lead to detrending issues in the yaw angle estimation. Finding alternative approaches or incorporating additional sensors or techniques to compensate for the lack of magnetometer data can help improve the accuracy of yaw estimation.

Integration with EMG: Integrating the IMU-based motion tracking system with EMG acquisition can provide a more comprehensive understanding of patients' muscle conditions and movement execution during rehabilitation therapy. This integration can enhance the analysis and monitoring capabilities of the system, enabling personalized therapy and objective progress evaluation.

By addressing these future work cues, the IMU-based motion tracking system can be further improved in terms of accuracy, reliability, and practical applicability in clinical settings. Combining advanced sensor calibration, optimized sensor fusion

algorithms, improved yaw detrending, and integration with EMG can enhance the system's overall performance and contribute to more effective and personalized rehabilitation therapy.

Bibliography

[1] Thomas Brunner, Jean-Philippe Lauffenburger, Sébastien Changey, and Michel Basset. «Magnetometer-augmented IMU simulator: In-depth elaboration». In: *Sensors* 15.3 (2015), pp. 5293–5310 (cit. on pp. 3, 4).

[2] Eric W Weisstein. «Rotation matrix». In: *https://mathworld. wolfram. com/* (2003) (cit. on p. 5).

[3] Richard Pio. «Euler angle transformations». In: *IEEE Transactions on automatic control* 11.4 (1966), pp. 707–715 (cit. on p. 5).

[4] Ma Myint Myint Aye. «Analysis of Euler angles in a simple two-axis gimbals set». In: *World Acad. Sci. Eng. Technol* 81 (2011), pp. 389–394 (cit. on p. 5).

[5] *MS Windows NT Kernel Description*. `https://i0.wp.com/www.mecharithm.com/wp-content/uploads/2021/07/ZYX-euler-angles-demonstration-1.png?w=1392&ssl=1`. Accessed: 2010-09-30 (cit. on p. 6).

[6] James Diebel et al. «Representing attitude: Euler angles, unit quaternions, and rotation vectors». In: *Matrix* 58.15-16 (2006), pp. 1–35 (cit. on pp. 7, 8).

[7] Serdar Kucuk and Zafer Bingul. *Robot kinematics: Forward and inverse kinematics*. INTECH Open Access Publisher London, UK, 2006 (cit. on p. 9).

[8] Hassen Fourati, Noureddine Manamanni, Lissan Afilal, and Yves Handrich. «A nonlinear filtering approach for the attitude and dynamic body acceleration estimation based on inertial and magnetic sensors: Bio-logging application». In: *IEEE Sensors Journal* 11.1 (2010), pp. 233–244 (cit. on p. 9).

[9] Mark Euston, Paul Coote, Robert Mahony, Jonghyuk Kim, and Tarek Hamel. «A complementary filter for attitude estimation of a fixed-wing UAV». In: *2008 IEEE/RSJ international conference on intelligent robots and systems*. IEEE. 2008, pp. 340–345 (cit. on p. 9).

[10] Yaguang Yang. «Spacecraft attitude determination and control: Quaternion based method». In: *Annual Reviews in Control* 36.2 (2012), pp. 198–219 (cit. on pp. 9, 18).

[11] W-W Wang and L-C Fu. «Mirror therapy with an exoskeleton upper-limb robot based on IMU measurement system». In: *2011 IEEE international symposium on medical measurements and applications*. IEEE. 2011, pp. 370–375 (cit. on p. 9).

[12] Carlos Cifuentes, Ariel Braidot, Luis Rodrıguez, Melisa Frisoli, Alfonso Santiago, and Anselmo Frizera. «Development of a wearable ZigBee sensor system for upper limb rehabilitation robotics». In: *2012 4th IEEE RAS & EMBS International Conference on Biomedical Robotics and Biomechatronics (BioRob)*. IEEE. 2012, pp. 1989–1994 (cit. on p. 9).

[13] Je-Nam Kim, Mun-Ho Ryu, Yoon-Seok Yang, and Tae-Koon Kim. «Upper extremity rehabilitation program using inertial sensors and virtual reality for patients with upper extremity hemiplegia due to disorders after stroke». In: *Proceedings of International Conference on Computer Science and Technology (CST'12)*. 2012, pp. 71–76 (cit. on p. 9).

[14] Jon Eriksson. «Hands-off robotics for post-stroke arm rehabilitation». In: *Technical Report* (2004) (cit. on p. 9).

[15] ZQ Ding, ZQ Luo, A Causo, IM Chen, KX Yue, SH Yeo, and KV Ling. «Inertia sensor-based guidance system for upperlimb posture correction». In: *Medical engineering & physics* 35.2 (2013), pp. 269–276 (cit. on p. 9).

[16] Gianni Fenu and Gary Steri. «IMU based post-traumatic rehabilitation assessment». In: *2010 3rd International Symposium on Applied Sciences in Biomedical and Communication Technologies (ISABEL 2010)*. IEEE. 2010, pp. 1–5 (cit. on p. 9).

[17] Yi-Chen Huang, Tsung-Long Chen, Bo-Chun Chiu, Chih-Wei Yi, Chung-Wei Lin, Yu-Jung Yeh, and Lun-Chia Kuo. «Calculate golf swing trajectories from imu sensing data». In: *2012 41st International Conference on Parallel Processing Workshops*. IEEE. 2012, pp. 505–513 (cit. on p. 9).

[18] Tung Mun Hon, SMN Arosha Senanayake, and Nick Flyger. «Biomechanical analysis of 10-pin bowling using wireless inertial sensor». In: *2009 IEEE/ASME International Conference on Advanced Intelligent Mechatronics*. IEEE. 2009, pp. 1130–1135 (cit. on p. 9).

[19] Ronald Azuma, Bruce Hoff, Howard Neely, and Ron Sarfaty. «A motion-stabilized outdoor augmented reality system». In: *Proceedings IEEE Virtual Reality (Cat. No. 99CB36316)*. IEEE. 1999, pp. 252–259 (cit. on p. 9).

[20] He Zhao and Zheyao Wang. «Motion measurement using inertial sensors, ultrasonic sensors, and magnetometers with extended kalman filter for data fusion». In: *IEEE Sensors Journal* 12.5 (2011), pp. 943–953 (cit. on p. 9).

[21] Norhafizan Ahmad, Raja Ariffin Raja Ghazilla, Nazirah M Khairi, and Vijayabaskar Kasi. «Reviews on various inertial measurement unit (IMU) sensor applications». In: *International Journal of Signal Processing Systems* 1.2 (2013), pp. 256–262 (cit. on pp. 9, 10).

[22] Rong Zhu and Zhaoying Zhou. «A real-time articulated human motion tracking using tri-axis inertial/magnetic sensors package». In: *IEEE Transactions on Neural systems and rehabilitation engineering* 12.2 (2004), pp. 295–302 (cit. on p. 10).

[23] Zakriya Mohammed, Ibrahim (Abe) M Elfadel, and Mahmoud Rasras. «Monolithic multi degree of freedom (MDoF) capacitive MEMS accelerometers». In: *Micromachines* 9.11 (2018), p. 602 (cit. on pp. 10, 13).

[24] Vittorio MN Passaro, Antonello Cuccovillo, Lorenzo Vaiani, Martino De Carlo, and Carlo Edoardo Campanella. «Gyroscope technology and applications: A review in the industrial perspective». In: *Sensors* 17.10 (2017), p. 2284 (cit. on pp. 11, 14, 15).

[25] Huikai Xie and Gary K Fedder. «Integrated microelectromechanical gyroscopes». In: *Journal of aerospace engineering* 16.2 (2003), pp. 65–75 (cit. on p. 14).

[26] Jason J Ford and Michael E Evans. «Online estimation of Allan variance parameters». In: *Journal of guidance, control, and dynamics* 23.6 (2000), pp. 980–987 (cit. on p. 15).

[27] Rudolph Emil Kalman et al. «A new approach to linear filtering and prediction problems [J]». In: *Journal of basic Engineering* 82.1 (1960), pp. 35–45 (cit. on p. 17).

[28] Mark Euston, Paul Coote, Robert Mahony, Jonghyuk Kim, and Tarek Hamel. «A complementary filter for attitude estimation of a fixed-wing UAV». In: *2008 IEEE/RSJ International Conference on Intelligent Robots and Systems*. 2008, pp. 340–345. DOI: 10.1109/IROS.2008.4650766 (cit. on pp. 17, 18).

[29] Daniel Weber, Clemens Gühmann, and Thomas Seel. «Neural networks versus conventional filters for inertial-sensor-based attitude estimation». In: *2020 IEEE 23rd International Conference on Information Fusion (FUSION)*. IEEE. 2020, pp. 1–8 (cit. on p. 18).

[30] Roberto G Valenti, Ivan Dryanovski, and Jizhong Xiao. «Keeping a good attitude: A quaternion-based orientation filter for IMUs and MARGs». In: *Sensors* 15.8 (2015), pp. 19302–19330 (cit. on p. 18).

[31] Gabriele Ligorio and Angelo M Sabatini. «A novel Kalman filter for human motion tracking with an inertial-based dynamic inclinometer». In: *IEEE Transactions on Biomedical Engineering* 62.8 (2015), pp. 2033–2043 (cit. on p. 18).

[32] Claudia Mazza, Marco Donati, John McCamley, Pietro Picerno, and Aurelio Cappozzo. «An optimized Kalman filter for the estimate of trunk orientation from inertial sensors data during treadmill walking». In: *Gait & posture* 35.1 (2012), pp. 138–142 (cit. on p. 18).

[33] James Calusdian, Xiaoping Yun, and Eric Bachmann. «Adaptive-gain complementary filter of inertial and magnetic data for orientation estimation». In: *2011 IEEE International Conference on Robotics and Automation*. IEEE. 2011, pp. 1916–1922 (cit. on p. 18).

[34] Sebastian OH Madgwick, Andrew JL Harrison, and Ravi Vaidyanathan. «Estimation of IMU and MARG orientation using a gradient descent algorithm». In: *2011 IEEE international conference on rehabilitation robotics*. IEEE. 2011, pp. 1–7 (cit. on pp. 18, 64).

[35] Alexander D Young. «Comparison of orientation filter algorithms for realtime wireless inertial posture tracking». In: *2009 Sixth International Workshop on Wearable and Implantable Body Sensor Networks*. IEEE. 2009, pp. 59–64 (cit. on p. 18).

[36] Robert Mahony, Tarek Hamel, and Jean-Michel Pflimlin. «Nonlinear complementary filters on the special orthogonal group». In: *IEEE Transactions on automatic control* 53.5 (2008), pp. 1203–1218 (cit. on p. 18).

[37] Daniel Roetenberg, Chris TM Baten, and Peter H Veltink. «Estimating body segment orientation by applying inertial and magnetic sensing near ferromagnetic materials». In: *IEEE transactions on neural systems and rehabilitation engineering* 15.3 (2007), pp. 469–471 (cit. on p. 18).

[38] Henk J Luinge and Peter H Veltink. «Inclination measurement of human movement using a 3-D accelerometer with autocalibration». In: *IEEE Transactions on neural systems and rehabilitation engineering* 12.1 (2004), pp. 112–121 (cit. on p. 18).

[39] Angelo M Sabatini. «Quaternion-based extended Kalman filter for determining orientation by inertial and magnetic sensing». In: *IEEE transactions on Biomedical Engineering* 53.7 (2006), pp. 1346–1356 (cit. on p. 18).

[40] Mahdi Abolfazli Esfahani, Han Wang, Keyu Wu, and Shenghai Yuan. «OriNet: Robust 3-D orientation estimation with a single particular IMU». In: *IEEE Robotics and Automation Letters* 5.2 (2019), pp. 399–406 (cit. on p. 18).

[41] Roberto G Valenti, Ivan Dryanovski, and Jizhong Xiao. «A linear Kalman filter for MARG orientation estimation using the algebraic quaternion algorithm». In: *IEEE Transactions on Instrumentation and Measurement* 65.2 (2015), pp. 467–481 (cit. on p. 18).

[42] Sumit Majumder and M Jamal Deen. «A robust orientation filter for wearable sensing applications». In: *IEEE Sensors Journal* 20.23 (2020), pp. 14228–14236 (cit. on p. 18).

[43] Michael B Del Rosario, Heba Khamis, Phillip Ngo, Nigel H Lovell, and Stephen J Redmond. «Computationally efficient adaptive error-state Kalman filter for attitude estimation». In: *IEEE Sensors Journal* 18.22 (2018), pp. 9332–9342 (cit. on p. 18).

[44] Bingfei Fan, Qingguo Li, and Tao Liu. «Improving the accuracy of wearable sensor orientation using a two-step complementary filter with state machine-based adaptive strategy». In: *Measurement Science and Technology* 29.11 (2018), p. 115104 (cit. on p. 18).

[45] Siwen Guo, Jin Wu, Zuocai Wang, Jide Qian, et al. «Novel MARG-sensor orientation estimation algorithm using fast Kalman filter». In: *Journal of Sensors* 2017 (2017) (cit. on p. 18).

[46] Thomas Seel and Stefan Ruppin. «Eliminating the effect of magnetic disturbances on the inclination estimates of inertial sensors». In: *IFAC-PapersOnLine* 50.1 (2017), pp. 8798–8803 (cit. on p. 18).

[47] Alberto Olivares, JM Górriz, Javier Ramırez, and Gonzalo Olivares. «Using frequency analysis to improve the precision of human body posture algorithms based on Kalman filters». In: *Computers in Biology and Medicine* 72 (2016), pp. 229–238 (cit. on p. 18).

[48] Panos Marantos, Yannis Koveos, and Kostas J Kyriakopoulos. «UAV state estimation using adaptive complementary filters». In: *IEEE Transactions on Control Systems Technology* 24.4 (2015), pp. 1214–1226 (cit. on p. 18).

[49] Marco Caruso, Angelo Maria Sabatini, Daniel Laidig, Thomas Seel, Marco Knaflitz, Ugo Della Croce, and Andrea Cereatti. «Analysis of the accuracy of ten algorithms for orientation estimation using inertial and magnetic sensing under optimal conditions: One size does not fit all». In: *Sensors* 21.7 (2021), p. 2543 (cit. on p. 18).

[50] Elena Bergamini, Gabriele Ligorio, Aurora Summa, Giuseppe Vannozzi, Aurelio Cappozzo, and Angelo Maria Sabatini. «Estimating orientation using magnetic and inertial sensors and different sensor fusion approaches: Accuracy assessment in manual and locomotion tasks». In: *Sensors* 14.10 (2014), pp. 18625–18649 (cit. on p. 18).

[51] Milad Nazarahari and Hossein Rouhani. «40 years of sensor fusion for orientation tracking via magnetic and inertial measurement units: Methods, lessons learned, and future challenges». In: *Information Fusion* 68 (2021), pp. 67–84 (cit. on p. 18).

[52] Sebastian Madgwick et al. «An efficient orientation filter for inertial and inertial/magnetic sensor arrays». In: *Report x-io and University of Bristol (UK)* 25 (2010), pp. 113–118 (cit. on pp. 19–21).

[53] Nils Büscher, Daniel Gis, Volker Kühn, and Christian Haubelt. «On the functional and extra-functional properties of IMU fusion algorithms for body-worn smart sensors». In: *Sensors* 21.8 (2021), p. 2747 (cit. on p. 20).

[54] Walter T Higgins. «A comparison of complementary and Kalman filtering». In: *IEEE Transactions on Aerospace and Electronic Systems* 3 (1975), pp. 321–325 (cit. on p. 22).

[55] Gianluca De Luca. *Fundamental concepts in EMG signal acquisition*. 2003 (cit. on p. 24).

[56] Bernabe Rodríguez-Tapia, Israel Soto, Daniela M. Martínez, and Norma Candolfi Arballo. «Myoelectric Interfaces and Related Applications: Current State of EMG Signal Processing–A Systematic Review». In: *IEEE Access* 8 (2020), pp. 7792–7805. DOI: 10.1109/ACCESS.2019.2963881 (cit. on p. 24).

[57] A Kolahi, Mo Hoviattalab, Tahmineh Rezaeian, M Alizadeh, M Bostan, and Hossein Mokhtarzadeh. «Design of a marker-based human motion tracking system». In: *Biomedical Signal Processing and Control* 2.1 (2007), pp. 59–67 (cit. on p. 25).

[58] Huiyu Zhou and Huosheng Hu. «Human motion tracking for rehabilitation—A survey». In: *Biomedical signal processing and control* 3.1 (2008), pp. 1–18 (cit. on p. 26).

[59] Rachel A Brady, Michael J Pavol, Tammy M Owings, and Mark D Grabiner. «Foot displacement but not velocity predicts the outcome of a slip induced in young subjects while walking». In: *Journal of biomechanics* 33.7 (2000), pp. 803–808 (cit. on p. 26).

[60] Pirjo Kejonen, Kari Kauranen, and Heikki Vanharanta. «The relationship between anthropometric factors and body-balancing movements in postural balance». In: *Archives of physical medicine and rehabilitation* 84.1 (2003), pp. 17–22 (cit. on p. 26).

[61] Juan Luis Jimenez Bascones. «Cloud point labelling in optical motion capture systems». In: 2019 (cit. on p. 26).

[62] Steve Bryson. «Virtual reality hardware». In: *Implementating Virtual Reality, ACM SIGGRAPH* 93 (1993), pp. 1–3 (cit. on p. 26).

[63] Ahmed Elhayek, Edilson de Aguiar, Arjun Jain, Jonathan Tompson, Leonid Pishchulin, Mykhaylo Andriluka, Christoph Bregler, Bernt Schiele, and Christian Theobalt. «Efficient ConvNet-based marker-less motion capture in general scenes with a low number of cameras». In: *2015 IEEE Conference on Computer Vision and Pattern Recognition (CVPR)* (2015), pp. 3810–3818 (cit. on p. 27).

[64] Yaqing Tao and Huosheng Hu. «Building a visual tracking system for home-based rehabilitation». In: *Proc. of the 9th Chinese Automation and Computing Society Conf. In the UK*. Vol. 20. Citeseer. 2003, pp. 343–448 (cit. on p. 27).

[65] Kamiar Aminian and Bijan Najafi. «Capturing human motion using body-fixed sensors: outdoor measurement and clinical applications». In: *Computer animation and virtual worlds* 15.2 (2004), pp. 79–94 (cit. on p. 27).

[66] S. Yabukami, H. Kikuchi, M. Yamaguchi, K.I. Arai, K. Takahashi, A. Itagaki, and N. Wako. «Motion capture system of magnetic markers using three-axial magnetic field sensor». In: *IEEE Transactions on Magnetics* 36.5 (2000), pp. 3646–3648. DOI: 10.1109/20.908928 (cit. on p. 28).

[67] Huiyu Zhou and Huosheng Hu. «Human motion tracking for rehabilitation—A survey». In: *Biomedical Signal Processing and Control* 3.1 (2008), pp. 1–18. ISSN: 1746-8094. DOI: https://doi.org/10.1016/j.bspc.2007.09.001. URL: https://www.sciencedirect.com/science/article/pii/S1746809407000778 (cit. on p. 28).

[68] Chenyu Gu, Weicong Lin, Xinyi He, Lei Zhang, and Mingming Zhang. «IMU-based Mocap system for rehabilitation applications: A systematic review». In: *Biomimetic Intelligence and Robotics* (2023), p. 100097 (cit. on p. 28).

[69] Kai-Nan An. «Kinematic analysis of human movement». In: *Annals of biomedical engineering* 12 (1984), pp. 585–597 (cit. on p. 30).

[70] Josefina Gutiérrez-Martınez, Ascención Ortiz-Espinosa, Pablo Rogelio Hernández-Rodrıguez, and Marco Antonio Núñez-Gaona. «System to measure the range of motion of the joints of the human hand.» In: *Revista de Investigacion Clinica; Organo del Hospital de Enfermedades de la Nutricion* 66 (2014), S122–30 (cit. on p. 30).

[71] Franklin P Mall. «On the angle of the elbow». In: *American journal of Anatomy* 4.4 (1905), pp. 391–404 (cit. on p. 30).

[72] Anouk M Oosterwijk, Marianne K Nieuwenhuis, Cees P van der Schans, and Leonora J Mouton. «Shoulder and elbow range of motion for the performance of activities of daily living: A systematic review». In: *Physiotherapy theory and practice* 34.7 (2018), pp. 505–528 (cit. on p. 30).

[73] Guoan Li, Thomas H Wuerz, and Louis E DeFrate. «Feasibility of using orthogonal fluoroscopic images to measure in vivo joint kinematics». In: *J. Biomech. Eng.* 126.2 (2004), pp. 313–318 (cit. on pp. 31, 32).

[74] Y Kikuchi, F Nakamura, H Wakiwaka, and H Yamada. «Index phase output characteristics of magnetic rotary encoder using a magneto-resistive element». In: *IEEE Transactions on Magnetics* 33.5 (1997), pp. 3370–3372 (cit. on pp. 31, 32).

[75] Richard L Gajdosik and Richard W Bohannon. «Clinical measurement of range of motion: review of goniometry emphasizing reliability and validity». In: *Physical therapy* 67.12 (1987), pp. 1867–1872 (cit. on pp. 31, 33).

[76] Emmanuel Roux, Stéphane Bouilland, A-P Godillon-Maquinghen, and Denis Bouttens. «Evaluation of the global optimisation method within the upper limb kinematics analysis». In: *Journal of biomechanics* 35.9 (2002), pp. 1279–1283 (cit. on pp. 31, 34).

[77] Hooman Dejnabadi, Brigitte M Jolles, Emilio Casanova, Pascal Fua, and Kamiar Aminian. «Estimation and visualization of sagittal kinematics of lower limbs orientation using body-fixed sensors». In: *IEEE transactions on biomedical engineering* 53.7 (2006), pp. 1385–1393 (cit. on pp. 31, 34).

[78] Takaomi Kojima, Yoshimi Kikuchi, Shigeo Seki, and Hiroyuki Wakiwaka. «Study on high accuracy optical encoder with 30 bits». In: *The 8th IEEE International Workshop on Advanced Motion Control, 2004. AMC'04.* IEEE. 2004, pp. 493–498 (cit. on pp. 32, 33).

[79] Morey J Kolber, Cydne Fuller, Jessica Marshall, Amanda Wright, and William J Hanney. «The reliability and concurrent validity of scapular plane shoulder elevation measurements using a digital inclinometer and goniometer». In: *Physiotherapy theory and practice* 28.2 (2012), pp. 161–168 (cit. on p. 33).

[80] Morey J. Kolber, Cydne Fuller, Jessica Marshall, Amanda Wright, and William J. Hanney. «The reliability and concurrent validity of scapular plane shoulder elevation measurements using a digital inclinometer and goniometer». In: *Physiotherapy Theory and Practice* 28.2 (2012). PMID: 21721999, pp. 161–168. DOI: 10.3109/09593985.2011.574203. eprint: https://doi.org/10.3109/09593985.2011.574203. URL: https://doi.org/10.3109/09593985.2011.574203 (cit. on p. 34).

[81] CW Spoor and FE Veldpaus. «Rigid body motion calculated from spatial co-ordinates of markers». In: *Journal of biomechanics* 13.4 (1980), pp. 391–393 (cit. on p. 34).

[82] Ralf Schmidt, Catherine Disselhorst-Klug, Jiri Silny, and Günter Rau. «A marker-based measurement procedure for unconstrained wrist and elbow motions». In: *Journal of biomechanics* 32.6 (1999), pp. 615–621 (cit. on p. 34).

[83] Greg Welch and Eric Foxlin. «Motion tracking: No silver bullet, but a respectable arsenal». In: *IEEE Computer graphics and Applications* 22.6 (2002), pp. 24–38 (cit. on p. 34).

[84] Hooman Dejnabadi, Brigitte M Jolles, and Kamiar Aminian. «A new approach to accurate measurement of uniaxial joint angles based on a combination of accelerometers and gyroscopes». In: *IEEE Transactions on Biomedical Engineering* 52.8 (2005), pp. 1478–1484 (cit. on p. 34).

[85] Karol J O'Donovan, Roman Kamnik, Derek T O'Keeffe, and Gerard M Lyons. «An inertial and magnetic sensor based technique for joint angle measurement». In: *Journal of biomechanics* 40.12 (2007), pp. 2604–2611 (cit. on p. 34).

[86] *MS Windows NT Kernel Description*. `http://www.qualisys.se/`. Accessed: 2010-09-30 (cit. on p. 35).

[87] *MS Windows NT Kernel Description*. `http://www.vicon.com/`. Accessed: 2010-09-30 (cit. on p. 35).

[88] Roy B Davis III, Sylvia Ounpuu, Dennis Tyburski, and James R Gage. «A gait analysis data collection and reduction technique». In: *Human movement science* 10.5 (1991), pp. 575–587 (cit. on p. 35).

[89] Huiyu Zhou, Huosheng Hu, Nigel D Harris, and Jackie Hammerton. «Applications of wearable inertial sensors in estimation of upper limb movements». In: *Biomedical Signal Processing and Control* 1.1 (2006), pp. 22–32 (cit. on p. 35).

[90] Alberto Esquenazi and Nathaniel H Mayer. «Instrumented assessment of muscle overactivity and spasticity with dynamic polyelectromyographic and motion analysis for treatment planning». In: *American journal of physical medicine & rehabilitation* 83.10 (2004), S19–S29 (cit. on p. 35).

[91] *MS Windows NT Kernel Description*. `http://www.ndigital.com/polaris.php`. Accessed: 2010-09-30 (cit. on p. 35).

[92] Won Jang and Miroslaw Skibniewski. «Embedded System for Construction Material Tracking Using Combination of Radio Frequency and Ultrasound Signal». In: (Nov. 2007) (cit. on p. 36).

[93] Michael J Caruso. «Applications of magnetic sensors for low cost compass systems». In: *IEEE 2000. Position location and navigation symposium (Cat. No. 00CH37062)*. IEEE. 2000, pp. 177–184 (cit. on p. 36).

[94] C Andersen. *A Survey of Gloves for Interaction with Virtual Worlds, Technicalreport* (cit. on p. 37).

[95] Michael J Bey, Stephanie K Kline, Roger Zauel, Terrence R Lock, and Patricia A Kolowich. «Measuring dynamic in-vivo glenohumeral joint kinematics: technique and preliminary results». In: *Journal of biomechanics* 41.3 (2008), pp. 711–714 (cit. on p. 39).

[96] Michael J Bey, Roger Zauel, Stephanie K Brock, and Scott Tashman. «Validation of a new model-based tracking technique for measuring three-dimensional, in vivo glenohumeral joint kinematics». In: (2006) (cit. on p. 39).

[97] Gonzalo Dominguez, Eladio Cardiel, Sandra Arias, and Pablo Rogeli. «A digital goniometer based on encoders for measuring knee-joint position in an orthosis». In: *2013 World Congress on Nature and Biologically Inspired Computing*. IEEE. 2013, pp. 1–4 (cit. on p. 39).

[98] *MS Windows NT Kernel Description*. `https://www.movella.com/products/wearables/xsens-mtw-awinda#overview`. Accessed: 2010-09-30 (cit. on p. 41).

[99] *MS Windows NT Kernel Description*. `https://www.microstrain.com/inertial-sensors/3dm-gq7`. Accessed: 2010-09-30 (cit. on p. 42).

[100] Grigore C Burdea. «Virtual rehabilitation–benefits and challenges». In: *Methods of information in medicine* 42.05 (2003), pp. 519–523 (cit. on p. 44).

[101] R. James Cotton and John Rogers. «Wearable Monitoring of Joint Angle and Muscle Activity». In: *2019 IEEE 16th International Conference on Rehabilitation Robotics (ICORR)*. 2019, pp. 258–263. DOI: `10.1109/ICORR.2019.8779538` (cit. on p. 44).

[102] Fabio Rossi, Andrea Mongardi, Paolo Motto Ros, Massimo Ruo Roch, Maurizio Martina, and Danilo Demarchi. «Tutorial: A versatile bio-inspired system for processing and transmission of muscular information». In: *IEEE Sensors Journal* 21.20 (2021), pp. 22285–22303 (cit. on p. 51).

[103] *MS Windows NT Kernel Description*. `https://www.microst.it/tutorial/spi_2.htm`. Accessed: 2010-09-30 (cit. on p. 55).

[104] Jared B Bancroft and Gérard Lachapelle. «Data fusion algorithms for multiple inertial measurement units». In: *Sensors* 11.7 (2011), pp. 6771–6798 (cit. on p. 56).

[105] Sara Stančin and Sašo Tomažič. «Time-and computation-efficient calibration of MEMS 3D accelerometers and gyroscopes». In: *Sensors* 14.8 (2014), pp. 14885–14915 (cit. on pp. 59, 60, 62).

[106] Sebastian OH Madgwick, Samuel Wilson, Ruth Turk, Jane Burridge, Christos Kapatos, and Ravi Vaidyanathan. «An extended complementary filter for full-body MARG orientation estimation». In: *IEEE/ASME Transactions on mechatronics* 25.4 (2020), pp. 2054–2064 (cit. on p. 63).

[107] Angelo Maria Sabatini. «Estimating three-dimensional orientation of human body parts by inertial/magnetic sensing». In: *Sensors* 11.2 (2011), pp. 1489–1525 (cit. on p. 64).

[108] Corrin P Walmsley, Sıan A Williams, Tiffany Grisbrook, Catherine Elliott, Christine Imms, and Amity Campbell. «Measurement of upper limb range of motion using wearable sensors: a systematic review». In: *Sports medicine-open* 4 (2018), pp. 1–22 (cit. on p. 70).

[109] Joshua A. Goreham, Kathleen F.E. MacLean, and Michel Ladouceur. «The validation of a low-cost inertial measurement unit system to quantify simple and complex upper-limb joint angles». In: *Journal of Biomechanics* 134 (2022), p. 111000. ISSN: 0021-9290. DOI: https://doi.org/10.1016/j.jbiomech.2022.111000. URL: https://www.sciencedirect.com/science/article/pii/S0021929022000562 (cit. on p. 70).

[110] Thiago Yukio Fukuda, Jorge Oliveira Echeimberg, José Eduardo Pompeu, Paulo Roberto Garcia Lucareli, Silvio Garbelotti, Rafaela Okano Gimenes, and Adilson Apolinário. «Root mean square value of the electromyographic signal in the isometric torque of the quadriceps, hamstrings and brachial biceps muscles in female subjects». In: *J Appl Res* 10.1 (2010), pp. 32–39 (cit. on p. 70).

[111] Simone Benatti, Filippo Casamassima, Bojan Milosevic, Elisabetta Farella, Philipp Schönle, Schekeb Fateh, Thomas Burger, Qiuting Huang, and Luca Benini. «A Versatile Embedded Platform for EMG Acquisition and Gesture Recognition». In: *IEEE Transactions on Biomedical Circuits and Systems* 9.5 (2015), pp. 620–630. DOI: 10.1109/TBCAS.2015.2476555 (cit. on p. 70).